Electronic Supplementary Material (ESI) for CrystEngComm.

Structures and Spin States of Crystalline [Fe(NCS)$_2$$L_2$] and [Fe$L_3$]$^{2+}$ Complexes (L = an Annelated 1,10-Phenanthroline Derivative)

Rafal Kulmaczewski and Malcolm A. Halcrow*

School of Chemistry, University of Leeds, Woodhouse Lane, Leeds LS2 9JT, UK.
E-mail: m.a.halcrow@leeds.ac.uk.

Supporting Information

Definitions of the structural distortion parameters discussed in the paper

Σ and Θ are defined as follows:

$$\Sigma = \sum_{i=1}^{12} \left| 90 - \beta_i \right| \qquad \Theta = \sum_{j=1}^{24} \left| 60 - \gamma_j \right|$$

where β_i are the twelve *cis*-N–Fe–N angles about the iron atom and γ_i are the 24 unique N–Fe–N angles measured on the projection of two triangular faces of the octahedron along their common pseudo-threefold axis (Scheme S1). Σ is a general measure of the deviation of a metal ion from an ideal octahedral geometry, while Θ more specifically indicates its distortion towards a trigonal prismatic structure. A perfectly octahedral complex gives $\Sigma = \Theta = 0$.

Σ and Θ were originally introduced to quantify small differences in the coordination geometries of high-spin iron(II) complexes of polydentate ligands.[1] More recently, they were popularised by Guionneau *et al.* as a way of confirming the spin state of a metal ion in a crystal structure; and to quantify the magnitude of the structural changes taking place during spin-crossover through $\Delta\Sigma$ and $\Delta\Theta$, the differences in these parameters between the high- and low-spin states of the complex.[2]

Because the high-spin state of a complex has a much more plastic structure than the low-spin, this is reflected in Σ and Θ which are usually much larger in the high-spin state. The absolute values of these parameters depend on the metal/ligand combination in the compound under investigation, however.[3] In general, complexes without conformationally restricted polydentate ligands can achieve geometries closer to an ideal octahedron, and give relatively small values of Σ and Θ as a result. Complexes of the $[Fe(NCS)_2(L)_2]$ type fall into this category.[2]

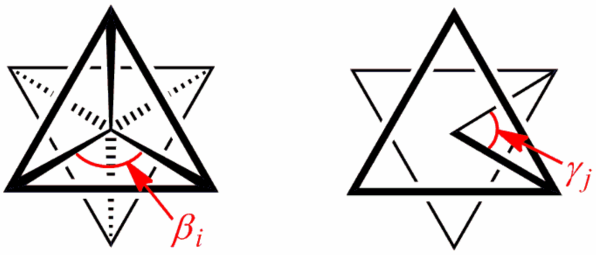

Scheme S1. Angles used in the definitions of the coordination distortion parameters Σ and Θ.

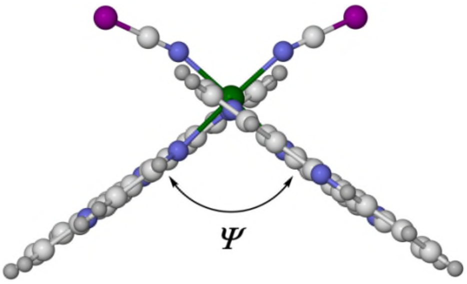

Figure S1 Structure of the $[Fe(NCS)_2(dppz)_2]$ molecule in (**2**·py), showing the definition of the Ψ parameter.[4] Colour code: C, white; Fe, green; N, blue; S, purple.

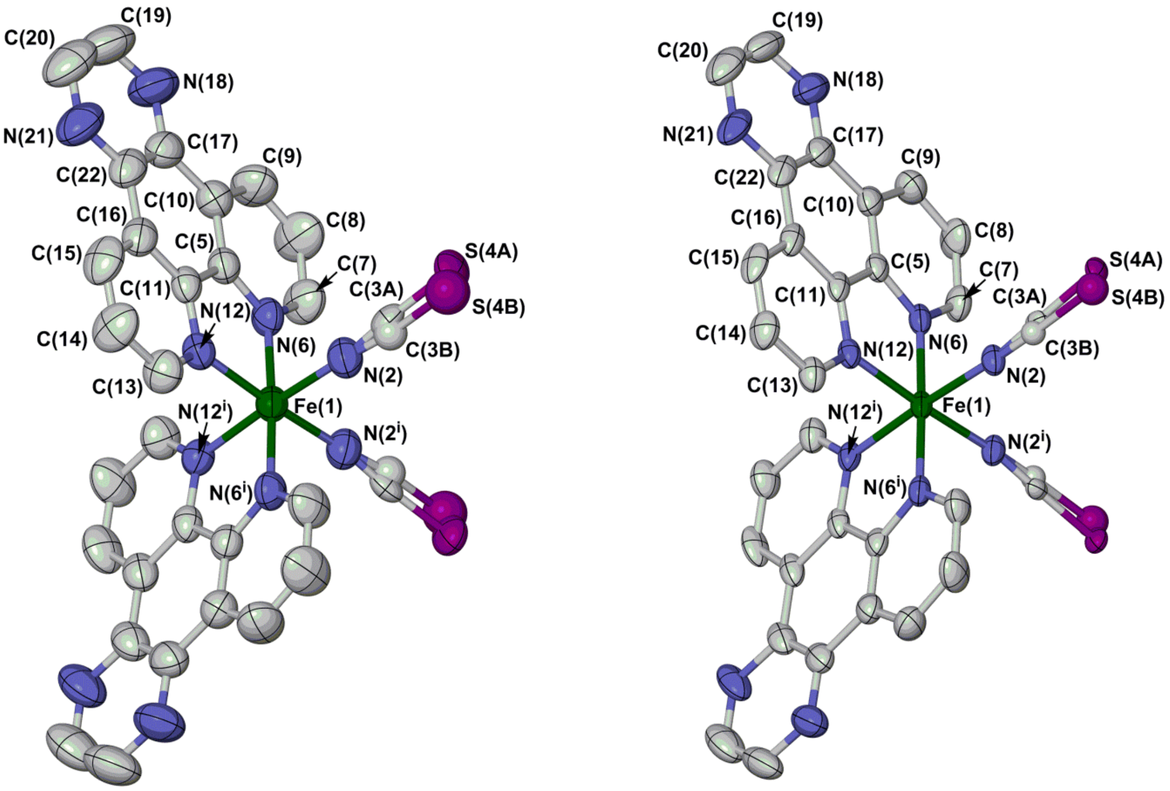

Figure S2. Comparison of the structures of the $[Fe(NCS)_2](dpq)_2]$ molecule in solvent-free **1** at 290 K (left) and 120 K (right). Displacement ellipsoids are at the 50 % probability level, and H atoms have been omitted for clarity. Symmetry code: (i) $-x, y, {}^{3}/_{2}-z$.

Colour code: C, white; Fe, green; N, blue; S, purple.

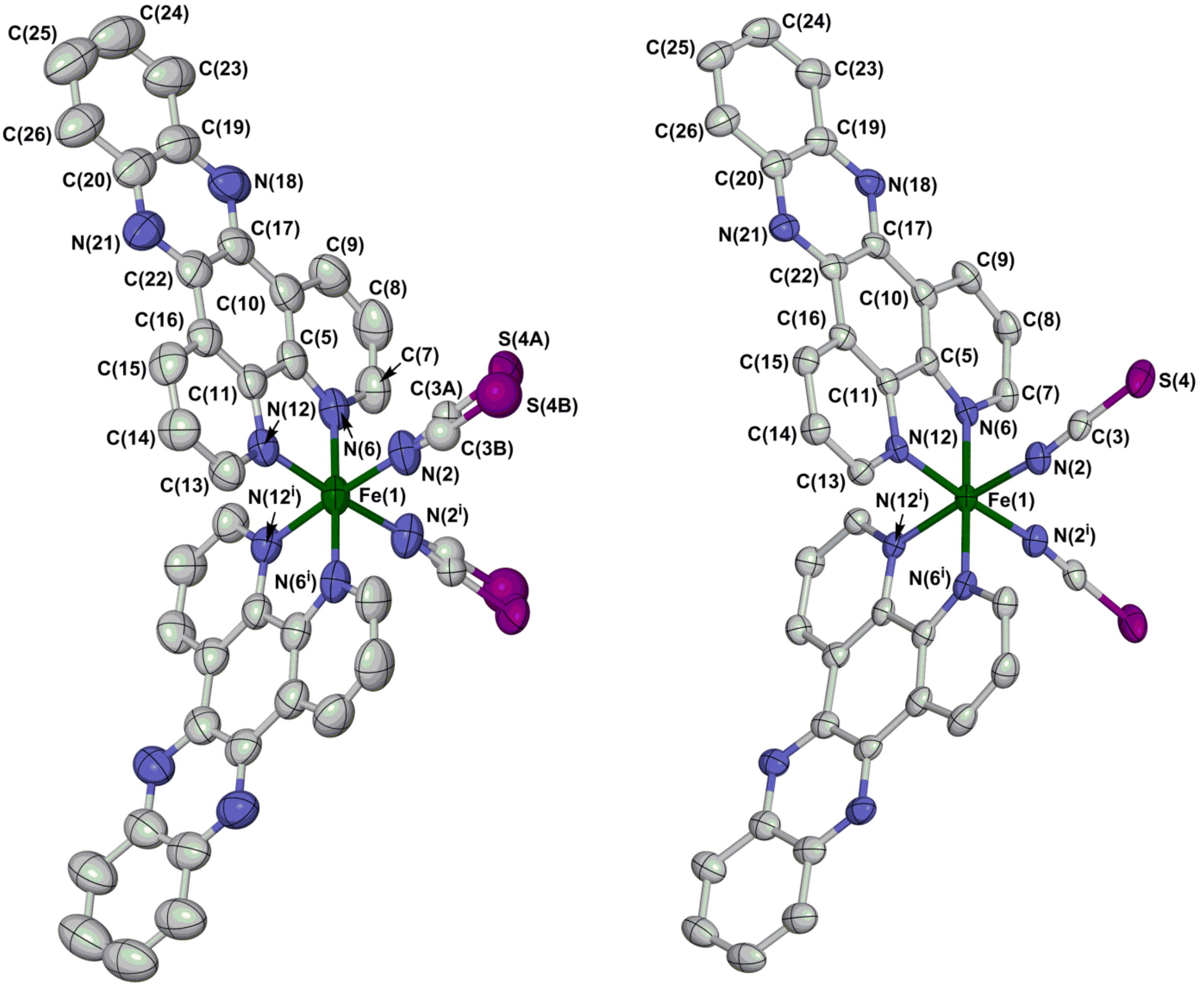

Figure S3. Comparison of the structures of the [Fe(NCS)$_2$](dppz)$_2$] molecule in solvent-free **2** at 290 K (left) and 120 K (right). Displacement ellipsoids are at the 50 % probability level, and H atoms have been omitted for clarity. Symmetry code: (i) –*x*, *y*, $^{3}/_{2}$–*z*.

Colour code: C, white; Fe, green; N, blue; S, purple.

The view at 120 K is the same as in Fig. 2 of the main article.

Table S1. Selected bond lengths (Å) and angles (°) for the crystal structures of solvent-free $[Fe(NCS)_2(dpq)_2]$ (**1**) and $[Fe(NCS)_2(dppz)_2]$ (**2**). See Figs. S2 and S3 for the atom numbering scheme employed. Symmetry code: (i) $-x, y, {}^3/_2-z$.

	1		**2**	
T [K]	120	290	100	290
Fe(1)–N(2)	1.934(2)	1.931(3)	1.938(3)	1.937(3)
Fe(1)–N(6)	1.964(2)	1.979(3)	1.968(3)	1.962(3)
Fe(1)–N(12)	1.958(2)	1.969(3)	1.966(3)	1.972(3)
N(2)–Fe(1)–N(2^i)	90.51(14)	90.50(17)	90.59(17)	90.47(19)
N(2)–Fe(1)–N(6)	87.78(10)	88.37(12)	87.21(12)	87.27(13)
N(2)–Fe(1)–N(12)	88.93(9)	89.11(11)	88.88(12)	88.81(12)
N(2)–Fe(1)–N(6^i)	93.43(10)	93.77(12)	93.19(12)	93.38(13)
N(2)–Fe(1)–N(12^i)	176.00(10)	175.60(12)	175.82(12)	175.70(13)
N(6)–Fe(1)–N(12)	82.59(10)	81.84(11)	82.65(11)	82.35(11)
N(6)–Fe(1)–N(6^i)	178.28(14)	176.96(15)	179.44(15)	179.07(16)
N(6)–Fe(1)–N(12^i)	96.21(10)	96.02(11)	96.96(11)	97.00(11)
N(12)–Fe(1)–N(12^i)	91.89(13)	91.62(15)	91.96(15)	92.23(15)
Fe(1)–N(2)–C(3)	165.6(7)/178.0(11)[a]	167.8(9)/175.9(14)[a]	169.2(3)	167.9(6)/174.9(9)[a]
N(2)–C(3)–S(4)	178.7(11)/177.3(16)[a]	167.8(9)/175.9(14)[a]	178.1(3)	177.2(8)/173.3(14)[a]

[a] The unique NCS^- ligand is disordered over two sites.

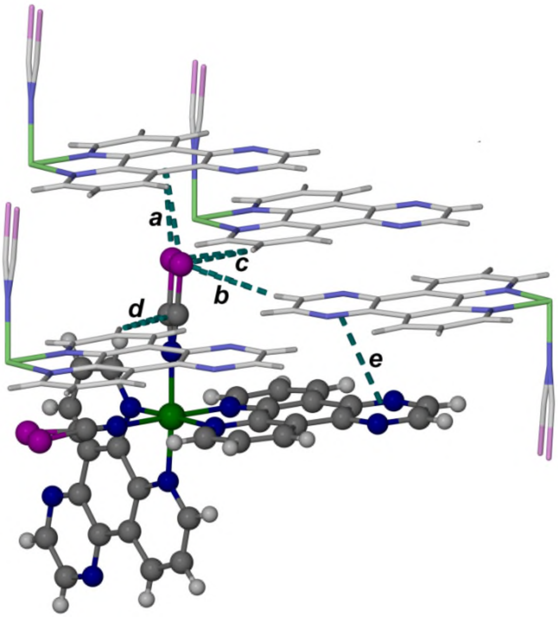

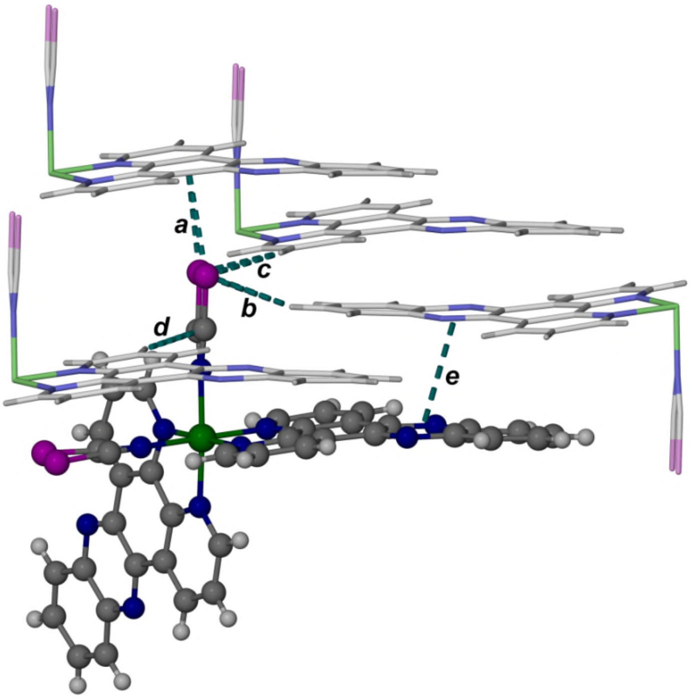

Figure S4. Views highlighting the unique short intermolecular contacts in the structures of **1** (top) and **2** (bottom) at 290 K. Both disorder sites of the NCS^- ligands are shown, but the symmetry-related interactions to the other NCS^- and dpq/dppz ligands in the C_2-symmetric molecule are not included, for clarity. The highlighted intermolecular distances are listed in Table S2.

Colour code: C, white or dark gray; H, pale gray; Fe, pale or dark green; N, pale or dark blue; S, pale or dark purple.

The view of **2** is the same as in Fig. 3 of the main article.

Table S2. Noteworthy intermolecular distances in **1** and **2**, highlighted in Fig. S4 (Å).
Symmetry codes: (ii) ½+*x*, –½+*y*, *z*; (iii) –1+*x, y, z*; (iv) –*x*, 2–*y*, –*z*; (v) ½+*x*, ½+*y*, *z*; (vi) –*x*, 1–*y*, 1–*z*.

1	S(4)…X(1^{ii})[a] ***a***	H(8)...S(4^{iii}) ***b***	H(19)...S(4^{iv}) ***c***	H(14)…C(3^{v}) ***d***	X(2)…X(2^{iv})[b] ***e***
T = 290 K[c]	3.12/3.14	2.91/3.10	2.93/3.19	2.85/2.86	3.44(1)
T = 120 K[c]	3.09/3.09	2.83/3.03	2.88/3.09	2.70/2.83	3.404(6)

2	S(4)…X(1^{ii}) ***a***	H(8)...S(4^{iii}) ***b***	H(25)...S(4^{vi}) ***c***	H(14)…C(3^{v}) ***d***	X(2)...X(2^{vi}) ***e***
T = 290 K[c]	3.07/3.10	2.89/3.19	3.02/3.53	2.76/2.93	3.534(7)
T = 120 K	3.04	3.04	3.06	2.73	3.477(4)

---

[a] X(1) is the centroid of phenylene ring [C(5), C(1), C(11), C(16), C(17), C(22)]. [b] X(2) is the centroid of the whole, unique dpq or dppz ligand. The value quoted is the distance between the least squares planes of the two dpq/dppz environments, which are strictly coplanar by symmetry. [c] The unique NCS^{-} ligand is disordered over two sites at this temperature.

Except for ***e***, all the contacts in the Table are more than 0.1 Å shorter than the sum of the van der Waals radii of the interacting groups in at least one of the structures. The relevant Pauling van der Waals radii are: H, 1.2 Å; S, 1.85 Å; arene ring, 1.7 Å [the radius of a thiocyanato C atom was also taken to be 1.7 Å].

The symmetry codes for the two compounds are slightly different, because the structures of **1** and **2** were merged to different origins by the diffractometer software.

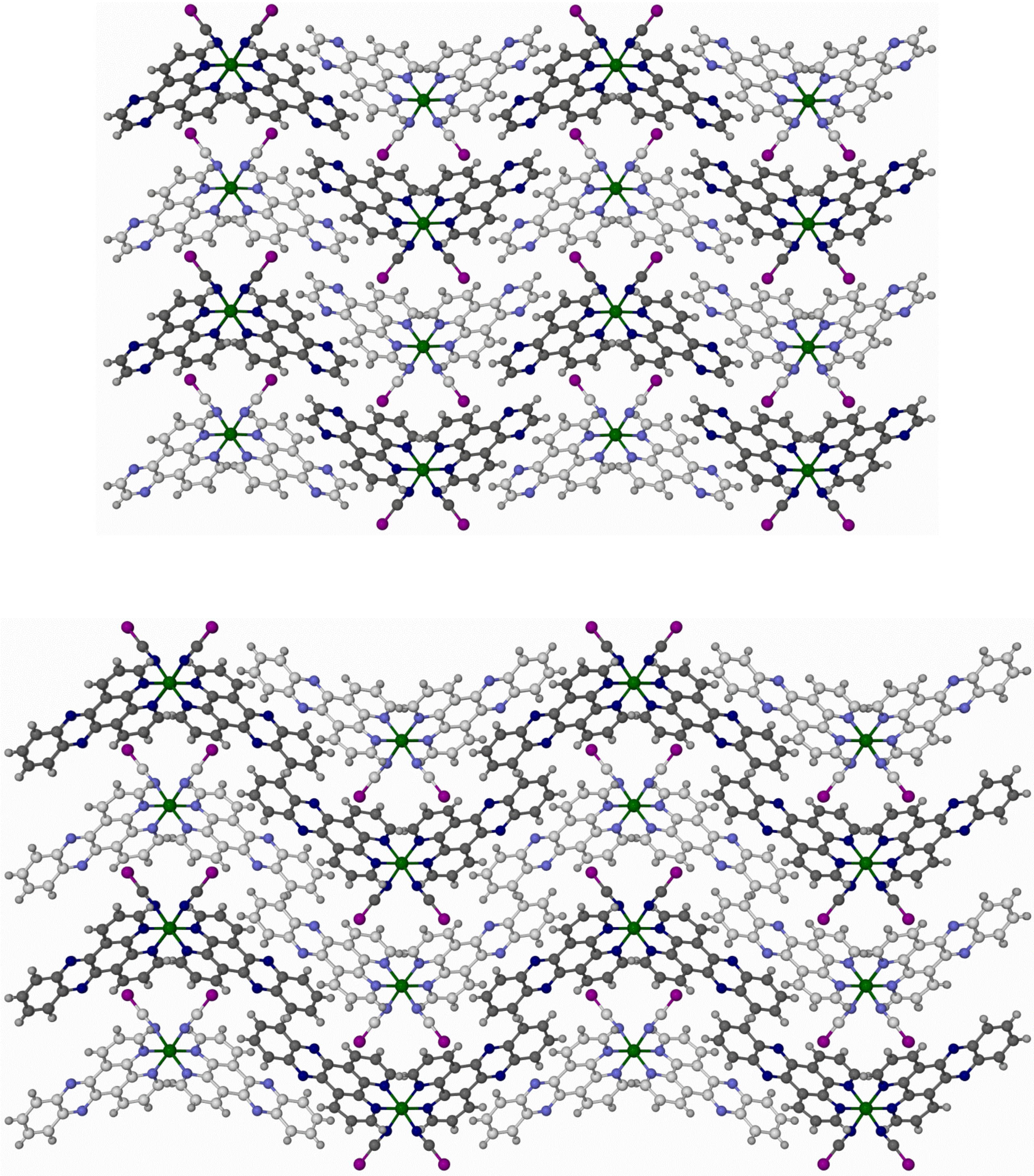

Figure S5. Packing diagrams of solvent-free **1** (top) and **2** (bottom). Only one orientation of disordered NCS^{-} ligands is shown, and alternate molecules have pale and dark colouration for clarity. The views are parallel to the crystallographic [100] vector, with *c* horizontal.

Colour code: C, white or dark gray; H, pale gray; Fe, green; N, pale or dark blue; S, purple.

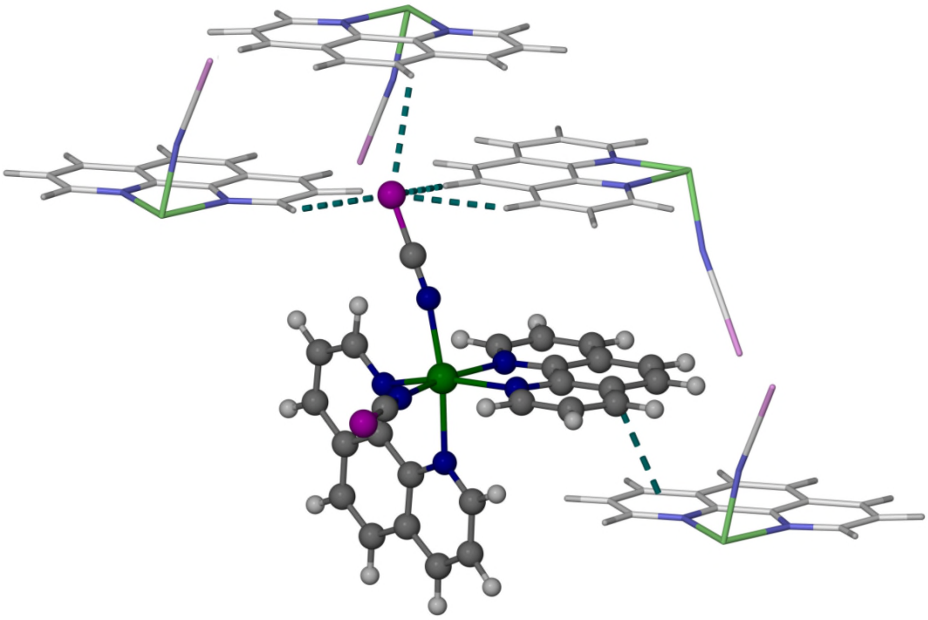

Figure S6. View highlighting the unique short intermolecular contacts in the literature structure of SCO-active [Fe(NCS)$_2$(phen)$_2$] at 290 K.[5] The symmetry-related interactions to the other NCS$^-$ and phen ligands in the *C*$_2$-symmetric molecule are not included, for clarity.

Colour code: C, white or dark gray; H, pale gray; Fe, pale or dark green; N, pale or dark blue; S, pale or dark purple.

Only contacts >0.1 Å shorter than the sum of the van der Waals radii of the interacting groups are highlighted. Clearly, the local environment about the NCS$^-$ ligand in this structure is less constrained than in the solvent-free phase of **1** and **2** (Fig. S3).

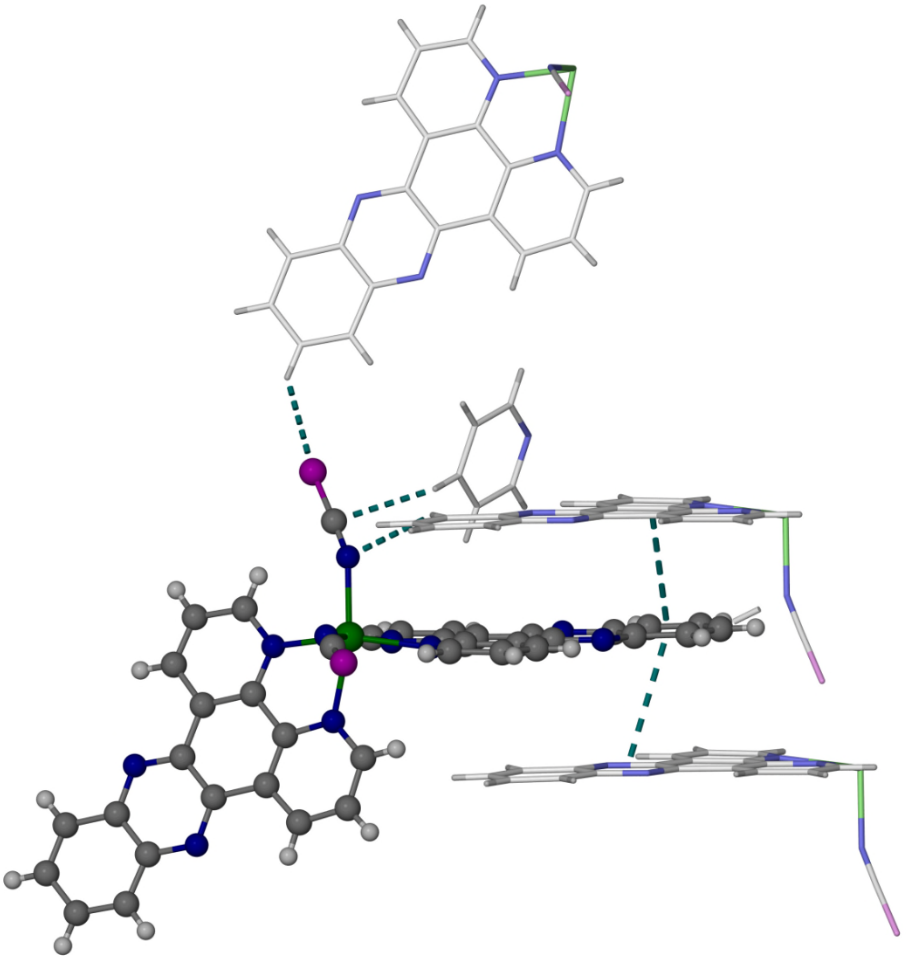

Figure S7. View highlighting the unique short intermolecular contacts in the literature structure of SCO-active **2**·py at 290 K.[4] The symmetry-related interactions to the other NCS– and dppz ligands in the *C*₂-symmetric molecule are not included, for clarity.

Colour code: C, white or dark gray; H, pale gray; Fe, pale or dark green; N, pale or dark blue; S, pale or dark purple.

Only contacts >0.1 Å shorter than the sum of the van der Waals radii of the interacting groups are highlighted. Clearly, the local environment about the NCS$^-$ ligand in this structure is less constrained than in the solvent-free phase of **1** and **2** (Fig. S4).

1·$2C_2H_4Cl_2$ (high-spin)

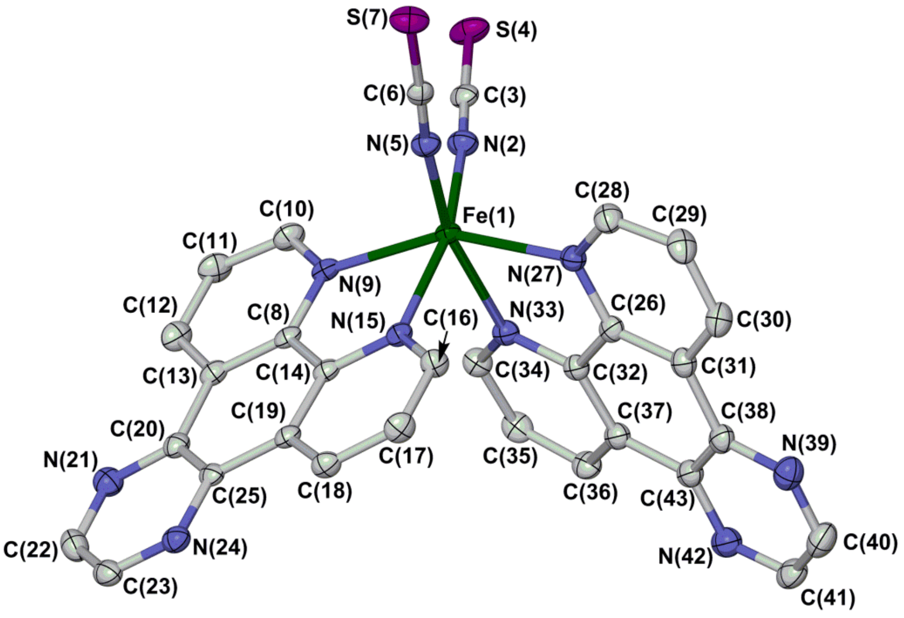

1·2py, 290 K (high-spin)

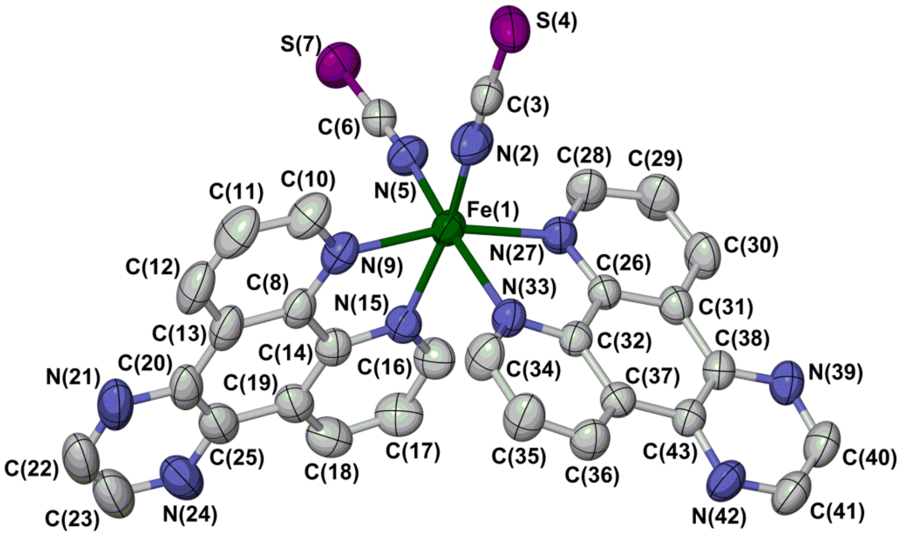

1·2py, 120 K (low-spin)

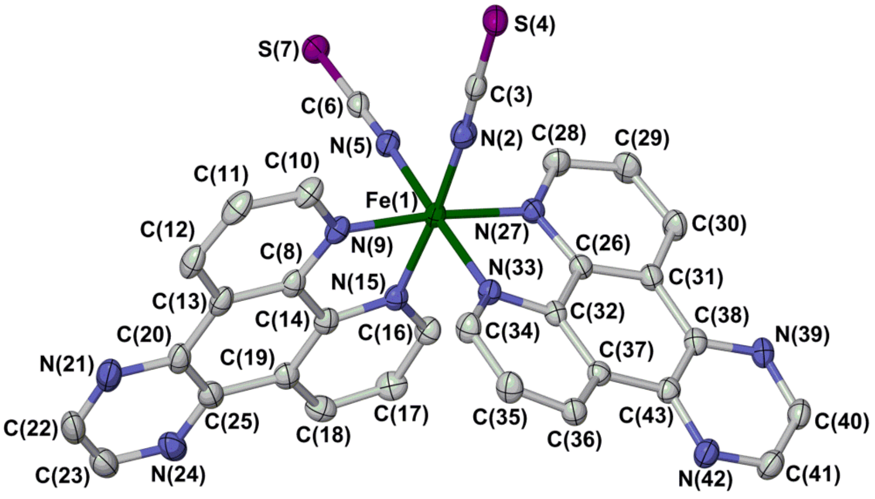

Figure S8. Comparison of the structures of the $[Fe(NCS)_2](dpq)_2]$ molecule in **1**·$2C_2H_4Cl_2$ at 100 K, and **1**·2py at 290 and 120 K. Displacement ellipsoids are at the 50 % probability level, and H atoms have been omitted for clarity.

Colour code: C, white; Fe, green; N, blue; S, purple.

Table S3. Selected bond lengths (Å) and angles (°) for the solvate crystal structures of [Fe(NCS)$_2$(dpq)$_2$] (**1**). See Fig. S8 for the atom numbering scheme employed.

	1·2$C_2H_4Cl_2$	**1**·2py				
T [K]	100	120	160	200	240	290
Fe(1)–N(2)	2.060(2)	1.9478(19)	1.961(3)	2.047(3)	2.075(4)	2.080(3)
Fe(1)–N(5)	2.092(2)	1.9656(18)	1.983(3)	2.047(3)	2.079(3)	2.093(2)
Fe(1)–N(9)	2.206(2)	1.9896(18)	2.029(3)	2.112(3)	2.173(3)	2.185(2)
Fe(1)–N(15)	2.226(2)	1.9897(17)	2.037(3)	2.143(2)	2.206(3)	2.221(2)
Fe(1)–N(27)	2.211(2)	1.9796(17)	2.017(3)	2.107(2)	2.161(3)	2.177(2)
Fe(1)–N(33)	2.234(2)	1.9932(17)	2.040(2)	2.146(2)	2.208(3)	2.235(2)
N(2)–Fe(1)–N(5)	93.59(9)	91.32(7)	92.13(11)	93.73(11)	94.95(14)	95.49(11)
N(2)–Fe(1)–N(9)	90.62(9)	92.11(7)	92.10(11)	92.33(11)	92.46(14)	92.61(10)
N(2)–Fe(1)–N(15)	164.88(9)	174.14(7)	172.76(11)	169.77(11)	168.20(14)	167.46(10)
N(2)–Fe(1)–N(27)	107.89(10)	92.15(7)	93.53(11)	96.54(11)	97.75(13)	98.03(10)
N(2)–Fe(1)–N(33)	92.20(9)	92.65(7)	93.21(11)	94.18(10)	94.88(13)	94.85(10)
N(5)–Fe(1)–N(9)	107.99(9)	90.30(7)	91.64(10)	94.61(10)	96.24(12)	96.80(9)
N(5)–Fe(1)–N(15)	90.05(9)	88.48(7)	88.54(10)	88.57(10)	88.43(12)	88.72(9)
N(5)–Fe(1)–N(27)	89.19(9)	93.17(7)	93.12(10)	93.13(9)	93.15(12)	93.14(9)
N(5)–Fe(1)–N(33)	163.54(9)	173.48(7)	171.56(10)	167.97(10)	165.64(13)	164.96(9)
N(9)–Fe(1)–N(15)	74.31(8)	82.03(7)	80.68(10)	77.54(9)	75.92(12)	75.14(9)
N(9)–Fe(1)–N(27)	154.13(8)	174.44(7)	172.48(10)	167.83(9)	165.48(12)	164.68(9)
N(9)–Fe(1)–N(33)	87.32(8)	94.73(7)	94.70(10)	94.11(9)	93.77(11)	93.62(8)
N(15)–Fe(1)–N(27)	86.81(9)	93.71(7)	93.63(10)	93.28(9)	93.34(12)	93.52(9)
N(15)–Fe(1)–N(33)	88.35(8)	88.10(7)	86.99(10)	85.23(9)	84.04(11)	83.49(8)
N(27)–Fe(1)–N(33)	74.37(9)	81.52(7)	80.02(10)	76.98(9)	75.16(11)	74.59(8)
Fe(1)–N(2)–C(3)	173.5(2)	175.49(17)	177.0(3)	179.7(3)	178.6(3)	177.7(3)
Fe(1)–N(5)–C(6)	174.4(2)	176.52(17)	176.4(3)	175.2(3)	174.6(3)	174.1(2)
N(2)–C(3)–S(4)	178.6(2)	178.55(19)	179.1(3)	178.9(3)	178.7(4)	178.9(3)
N(5)–C(6)–S(7)	179.7(2)	179.6(2)	179.5(3)	179.8(3)	179.1(4)	179.3(3)

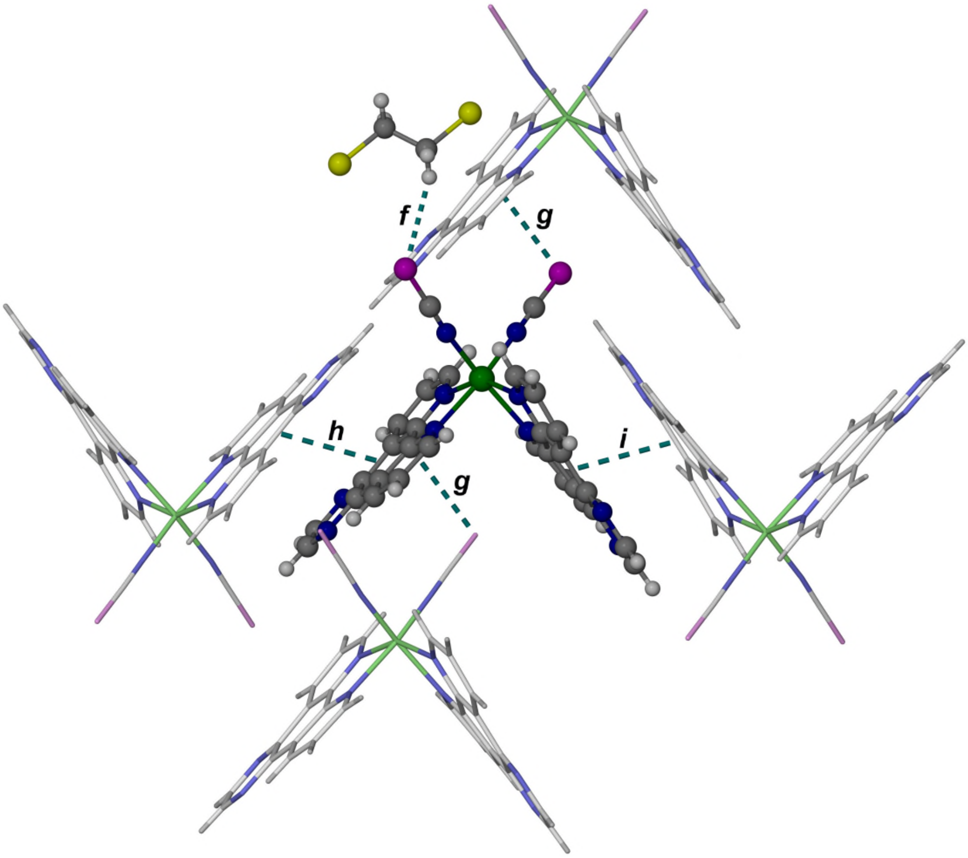

Figure S9. Views highlighting the unique short intermolecular contacts in the structure of **1**·$2C_2H_4Cl_2$. Solvent molecules that do not take part in these interactions have been omitted for clarity. The highlighted intermolecular distances are listed in Table S4.

Colour code: C, white or dark gray; H, pale gray; Cl, yellow; Fe, pale or dark green; N, pale or dark blue; S, pale or dark purple.

Table S4. Noteworthy intermolecular distances in **1**·$2C_2H_4Cl_2$, highlighted in Fig. S9 (Å). Symmetry codes: (iii) –1+*x*, *y*, *z*; (vii) 2–*x*, 1–*y*, 1–*z*; (viii) 1–*x*, –*y*, –*z*.

S(4)…C(14^{iii})[a] ***f***	H(45A)...S(7) ***g***	X(3)...X(3^{vii})[a,b] ***h***	X(4)…X(4^{viii})[b,c] ***i***
3.399(3)	2.92	3.330(4)	3.332(2)

[a] X(3) is the centroid of the whole dpq ligand C(8)-C(25). [b] The value quoted is the distance between the least squares planes of the two dpq environments, which are strictly coplanar by symmetry. [c] X(4) is the centroid of the other dpq ligand, C(26)-C(43).

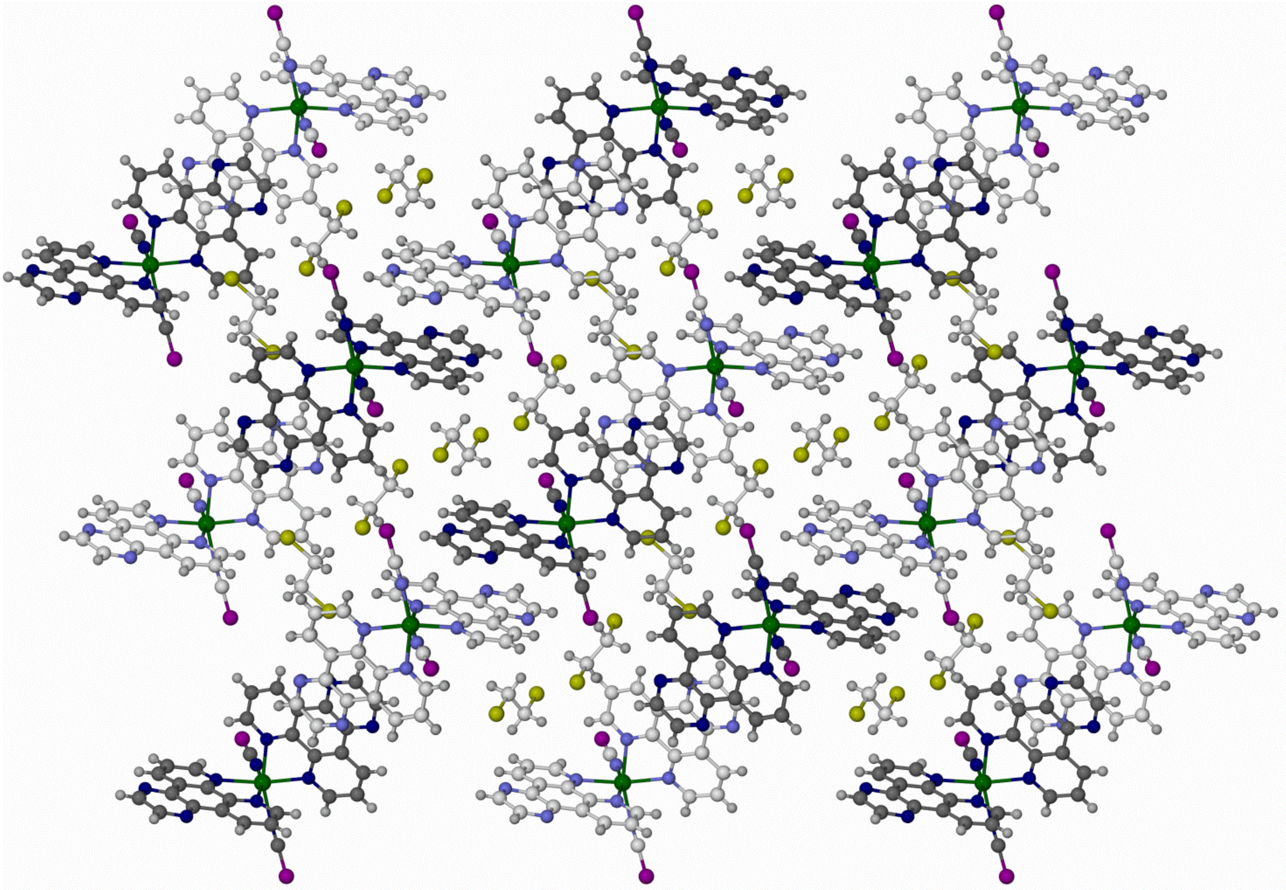

Figure S10. Packing diagram of **1**·2$C_2H_4Cl_2$. Only one orientation of disordered 1,2-dichloroethane solvent site is shown, and alternate complex molecules have pale and dark colouration for clarity. The view is parallel to the crystallographic [100] vector, with *c* horizontal.

Colour code: C, white or dark gray; H, pale gray; Cl, yellow; Fe, green; N, pale or dark blue; S, purple.

Molecules of **1** associate through π-stacking into 1D chains parellel to [011], which are in turn linked into sheets by weak intermolecular C–H...S contacts (perpendicular to the view). The sheets of complex molecules are separated by well-defined layers of 1,2-dichloroethane solvent.

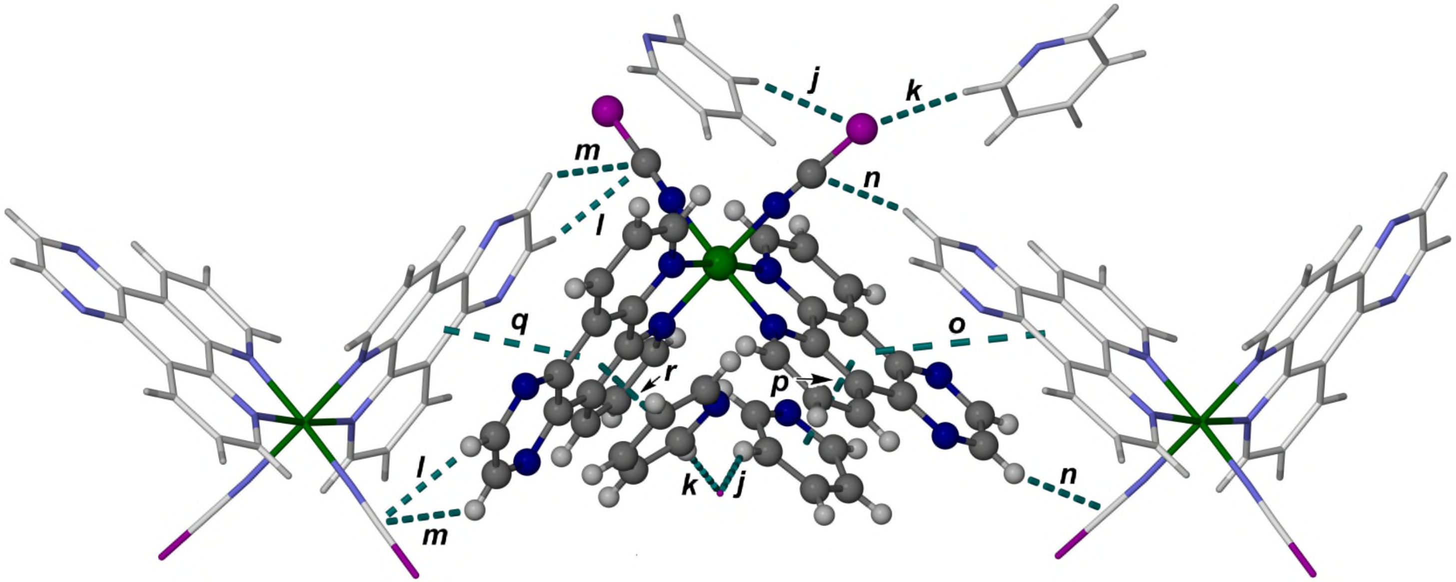

Figure S11. Views highlighting the unique short intermolecular contacts in the structure of **1**·2py. The highlighted intermolecular distances are listed in Table S5. Only one orientation of the disordered pyridine solvent molecule is shown, for clarity.

Colour code: C, white or dark gray; H, pale gray; Fe, pale or dark green; N, pale or dark blue; S, pale or dark purple.

Table S5. Noteworthy intermolecular distances in the high-spin and low-spin forms of **1**·2py, highlighted in Fig. S11 (Å, °). Symmetry codes: (ix) ½+*x*, $^{3}/_{2}$–*y*, ½+*z*; (x) 1–*x*, 1–*y*, 1–*z*; (xi) –*x*, 2–*y*, 1–*z*.

	H(48)…S(7^{ix})	H(51)...S(7^{ix})	H(40)...C(3^{x})	H(41)...C(3^{x})	H(23)...C(6^{xi})	X(5)…X(5^{xi})[a,b]	X(5)…X(6)[a,c,d]	X(7)…X(7^{x})[b,e]	X(7)…X(8)[d,e,f]
	j	***k***	***l***	***m***	***n***	***o***	***p***	***q***	***r***
T = 290 K	3.00	3.00/3.30[g]	2.82	2.87	2.90	3.36(1)	3.48(1), 3.2(2)	3.372(7)	3.54(2), 15.3(3)/ 3.06(3), 10.7(5)
T = 120 K	2.94	2.97/3.30[g]	2.74	2.74	2.83	3.282(7)	3.419(7), 2.0(1)	3.295(5)	3.40(1), 13.8(2)/ 2.95(2), 12.4(2)

[a]X(5) is the centroid of the whole dpq ligand C(8)-C(25). [b]The value quoted is the distance between the least squares planes of the two dpq environments, which are strictly coplanar by symmetry. [c]X(6) is the centroid of the pyridine ring N(44)-C(49). [d]The average interatomic distance and dihedral angle between the planes of these (non-coplanar) groups are given. [e]X(7) is the centroid of the whole dpq ligand C(26)-C(43). [f]X(8) is the centroid of the pyridine ring N(50)-C(55), which is disordered at all the temperatures studied. [g]This C–H group is part of the disordered pyridine solvent molecule.

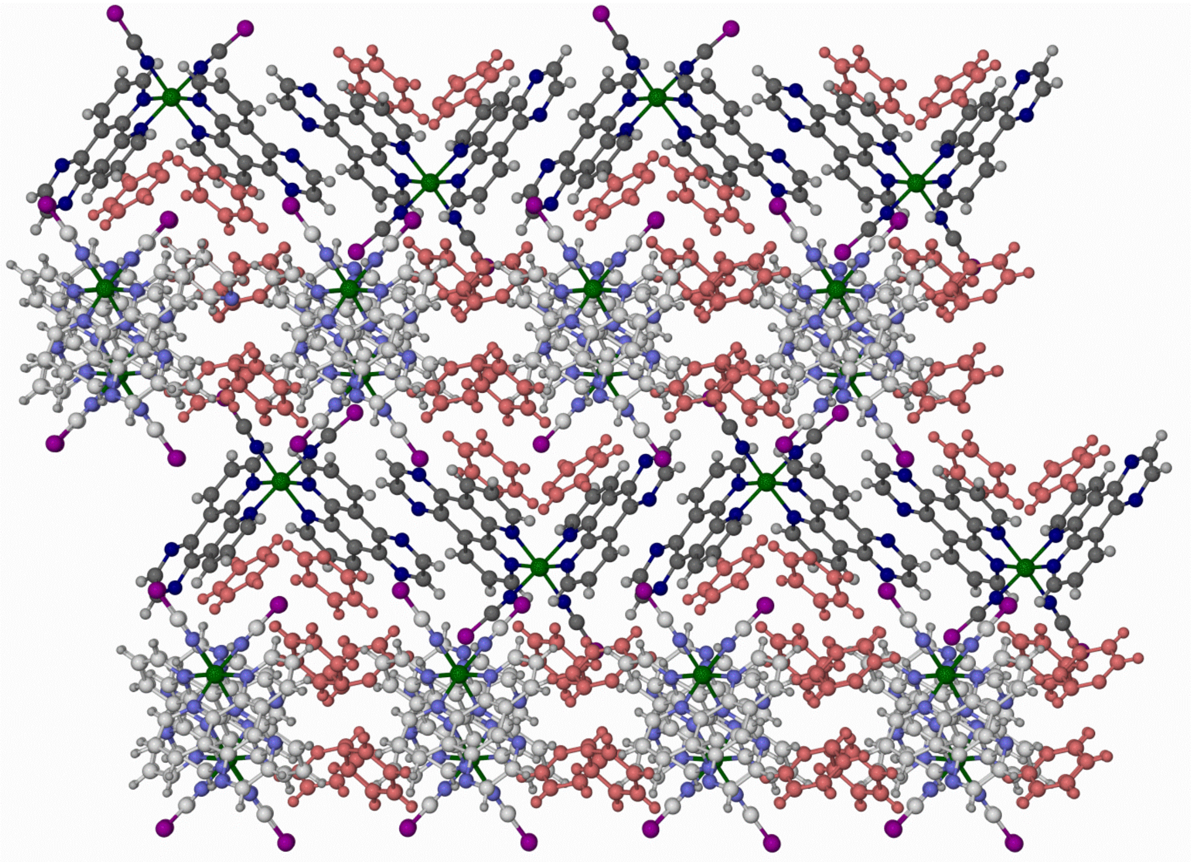

Figure S12. Packing diagram of **1**·2py. Only one orientation of the disordered pyridine molecule is included, for clarity. Alternate layers of π-stacked chains of complex molecules have pale and dark colouration for clarity, and the pyridine solvent is coloured red. The view is parallel to the crystallographic [110] vector.

Colour code: C, white or dark gray; H, pale gray; Cl, yellow; Fe, green; N, pale or dark blue; S, purple; pyridine molecules, red.

Molecules of **1** in this crystal associate through π-stacking into 1D chains, arranged in mutually perpendicular rows parallel to $\{\bar{1}10\}$. There are no short intermolecular interactions between these chains, which are separated by the solvent molecules.

Table S6. Variable temperature unit cell data for **1**·2py. These data are plotted in Fig. S13.

T [K]	a [Å]	b [Å]	c [Å]	β [°]	V [Å^3]
120	13.321(9)	16.188(8)	17.479(11)	109.91(6)	3544(10)
140	13.360(8)	16.199(8)	17.516(11)	110.05(6)	3561(10)
160	13.400(8)	16.212(8)	17.554(9)	110.17(5)	3579(9)
180	13.437(7)	16.257(7)	17.625(8)	110.23(4)	3613(8)
200	13.463(7)	16.272(7)	17.682(7)	110.24(4)	3634(8)
220	13.473(7)	16.289(7)	17.735(7)	110.30(4)	3650(8)
240	13.489(7)	16.301(7)	17.781(7)	110.32(4)	3667(8)
260	13.518(7)	16.288(7)	17.779(7)	110.45(4)	3668(8)
280	13.571(6)	16.283(6)	17.786(7)	110.49(4)	3682(7)

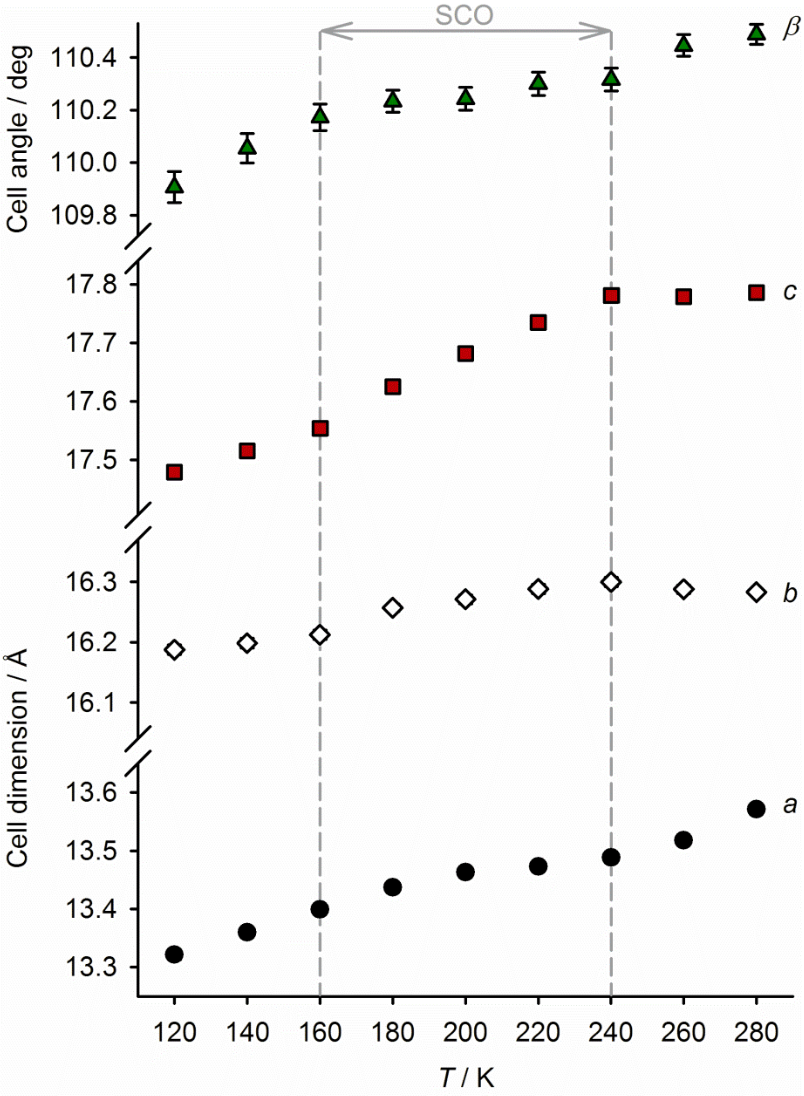

Figure S13. Variable temperature unit cell parameters for **1**·2py. These data are listed in Table S6.

The dashed lines highlight discontinuities in these data, which occur at temperatures corresponding to the approximate start and end points of the SCO transition (*cf* Fig. 4, main article).

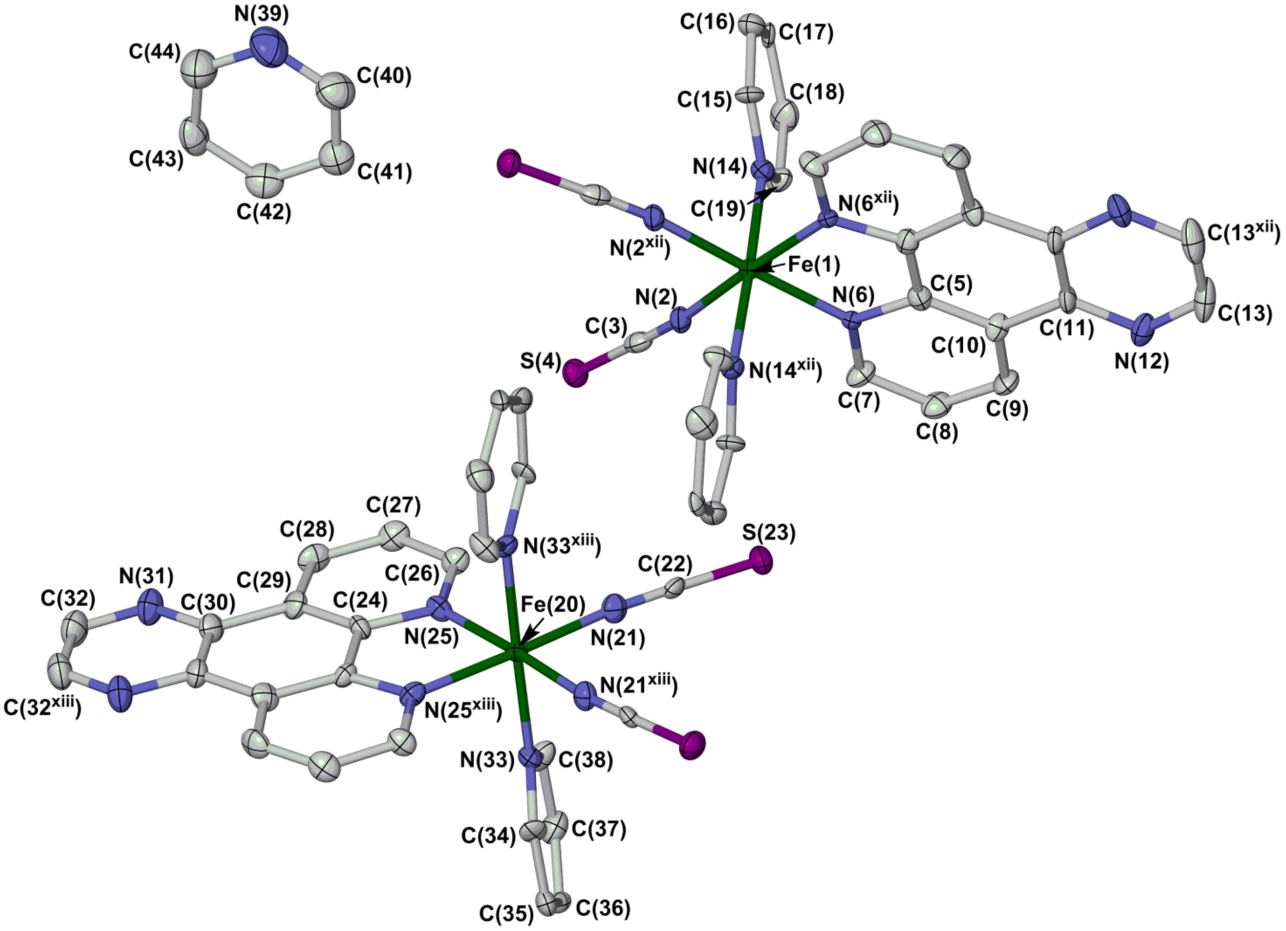

Figure S14. View of the asymmetric unit of $[Fe(NCS)_2(py)_2(dpq)]\cdot py$, from a partial refinement of a twinned dataset. Displacement ellipsoids are at the 50 % probability level, and H atoms have been omitted for clarity. Symmetry codes: (xii) $^{3}/_{2}–x, y, ^{1}/_{2}–z$; (xiii) $^{1}/_{2}–x, y, ^{1}/_{2}–z$.

Colour code: C, white; Fe, green; N, blue; S, purple.

Crystallographic details: $C_{31}H_{24}FeN_9S_2$, $M_r = 642.57$, monoclinic, $P2/n$, $a = 12.4914(11)$, $b = 13.6836(9)$, $c = 17.1800(12)$ Å, $\beta = 104.523(8)°$, $V = 3380.0(11)$ Å^3, $Z = 4$, $T = 120(2)$ K, μ(Cu-K_a) = 5.952 mm^{-1}, 11588 measured reflections, 5599 unique reflections, $R_{int} = 0.067$, R_1 ($I > 2\sigma(I)$) = 0.177, wR_2 (all data) = 0.433, GoF = 2.745.

The Fe–N bond lengths in this structure range from 1.961(9)-2.034(9) Å, showing that both half-molecules are fully low spin at 120 K.

This twinned structure has not been deposited with the CCDC.

Synthesis of bulk samples of [Fe(NCS)$_2$*L*$_2$] (L = dpq, 1; L = dppz, 2; L = dppn, 3).

Method 1 The same method, described here for compound **1**, was followed for each of **1-3** using an appropriate amount of the relevant ligand. A solution of Fe[NCS]$_2$ was prepared *in situ* by reacting Fe[ClO$_4$]$_2$·6H$_2$O (0.08 g, 0.22 mmol) and NBu$_4$NCS (0.13 g, 0.43 mmol) in acetone (10 cm^3). The mixture was stirred at room temperature for 30 min. A warm suspension of dpq (0.10 g, 0.43 mmol) in acetone (10 cm^3) was then added, leading to the rapid formation of a black precipitate. The solid was collected by filtration, and washed copiously with acetone until the washings were colourless. Yields 55-66 %.

1·2H$_2$O**:** Found C, 53.6; H, 2.60; N, 20.7 %. Calcd for $C_{30}H_{16}N_{10}FeS_2$·2H$_2$O C, 53.6; H, 3.00; N, 20.8 %. IR: *ν*{NCS} 2055w, 2110s cm^{-1}.[7]

2·1.5H$_2$O**:** Found C, 59.7; H, 2.70; N, 18.2 %. Calcd for $C_{38}H_{20}N_{10}FeS_2$·1.5H$_2$O C, 59.8; H, 3.04; N, 18.3 %. IR: *ν*{NCS} 2056w, 2112s cm^{-1}.[7]

3·2H$_2$O**:** Found C, 63.2; H, 2.80; N, 15.8 %. Calcd for $C_{46}H_{24}N_{10}FeS_2$·2H$_2$O C, 63.3; H, 3.23; N, 16.0 %. IR: *ν*{NCS} 2060w, 2109s cm^{-1}.[7]

Method 2. A solution of Fe[NCS]$_2$ was prepared by mixing Fe[ClO$_4$]2·6H$_2$O with KNCS in methanol (10 cm^3), and removing the KClO$_4$ precipitate by filtration. A solution of *L* (2 equiv) in 9:1 dichloromethane:methanol (20 cm^3) was then added dropwise to this mixture, and the resultant dark suspension was stirred for 30 min. The black solid was collected by filtration and washed with dichloromethane and methanol until the washings were colourless. Yields 34-49 %.

1·0.5H$_2$O**:** Found C, 55.4; H, 2.50; N, 21.7 %. calcd. for $C_{30}H_{16}N_{10}FeS_2$·0.5H$_2$O C, 55.8; H, 2.65; N, 21.7 %. IR: *ν*{NCS} 2062s cm^{-1}.[7] In contrast to all the other samples in this work, this material is predominantly high-spin at room temperature (Fig. S14).

3·2.5H$_2$O**:** Found C, 62.3; H, 2.80; N, 15.5 %. Calcd for $C_{46}H_{24}N_{10}FeS_2$·2.5H$_2$O C, 62.7; H, 3.32; N, 15.9 %. IR: *ν*{NCS} 2058w, 2111s cm^{-1}.[7]

Method 3. A solution of *L* (0.05 g) of 1,2-dichloroethane (5 cm^3) was poured into a standard test tube. Methanol (3 cm^3) was slowly deposited onto this solution as a middle-buffer layer. Finally, a methanol (3 cm^3) solution of Fe[NCS]$_2$, prepared as for Method 2, was introduced. Dark purple or black polycrystalline material usually appeared after 3-8 days, which sometimes also contained single crystals which were analysed by X-ray diffraction. Omission of the mid-layer solvent buffer from these layerings led to rapid precipitation of the products as black powders. Black single crystals of solvent-free **1**, **2** and **4**, and of **1**·2C$_2$H$_4$Cl$_2$, were sometimes obtained by this method but the bulk polycrystalline materials analysed with a hemihydrate formulation. Combined yields 34-49 %.

1·0.5H$_2$O**:** Found C, 55.7; H, 2.50; N, 21.6 %. Calcd for $C_{30}H_{16}N_{10}FeS_2$·0.5H$_2$O C, 55.8; H, 2.65; N, 21.7 %. IR: *ν*{NCS} 2060w, 2105s cm^{-1}.[7]

2·0.5H$_2$O**:** Found C, 61.3; H, 2.70; N, 19.0 %. Calcd for $C_{38}H_{20}N_{10}FeS_2$·0.5H$_2$O C, 61.2; H, 2.84; N, 18.8 %. IR: *ν*{NCS} 2046w, 2109s cm^{-1}.[7]

3·1.5H$_2$O**:** Found C, 63.9; H, 2.90; N, 15.9 %. Calcd for $C_{46}H_{24}N_{10}FeS_2$·1.5H$_2$O C, 64.0; H, 3.15; N, 16.2 %. IR: *ν*{NCS} 2055w, 2109s cm^{-1}.[7]

Synthesis of $[Fe(dppz)_3][ClO_4]_2$ (4)

A bulk sample of this complex was prepared as follows, for comparison with the single crystals that were originally obtained serendipitously (see above). Solutions of dppz (0.05 g, 0.18 mmol) in 1,2-dichloroethane, and $Fe[ClO_4]_2 \cdot 6H_2O$ (0.021 g, 0.06 mmol) in methanol, were layered as described for Method 3. This yielded dark red crystals of **4** after a period of days. Yield 0.045 g, 68 %. Found C, 58.3; H, 2.60; N, 15.2 %. Calcd for $C_{54}H_{30}Cl_2FeN_{12}O_8$ C, 58.9; H, 2.74; N, 15.3 %. HR-ESI MS *m*/*z* 451.1049 (calcd for $[Fe(dppz)_3]^{2+}$ 451.1028).

Synthesis of $[Fe(dppn)_3][BF_4]_2$ (5)

This was prepared as described for **4**, using dppn (0.05 g, 0.15 mmol) and $Fe[BF_4]_2 \cdot 6H_2O$ (0.017 g, 0.05 mmol). The complex was obtained as dark red microcrystals. Yield 0.059 g, 78 %. Microanalysis implied that the bulk polycrystalline material contained 1,2-dichloroethane, in contrast to the crystal used for the structure determination whose *SQUEEZE* analysis was inconsistent with the presence of a chlorinated solvent. Found C, 56.6; H, 2.95; N, 11.8 %. Calcd for $C_{66}H_{36}B_2F_8FeN_{12} \cdot 2C_2H_4Cl_2 \cdot 4H_2O$ C, 56.9; H, 3.41; N, 11.4 %. HR-ESIMS *m*/*z* 526.1275 (calcd for $[Fe(dppn)_3]^{2+}$ 526.1263).

Other measurements

Elemental microanalyses were performed by the University of Leeds School of Chemistry microanalytical service. Magnetic susceptibility measurements were performed with freshly isolated, unground polycrystalline samples, using a Quantum Design SQUID/VSM magnetometer in an applied field of 5000 G and a temperature ramp of 5 K min^{-1}. Diamagnetic corrections for the samples were estimated from Pascal’s constants;[6] a previously measured diamagnetic correction for the sample holder was also applied to the data. X-ray powder diffraction patterns were measured from ground polycrystalline samples, with a Bruker D2 Phaser diffractometer using Cu-$K\alpha$ radiation (λ = 1.5418 Å). Infrared spectra were recorded over the range 4000–400 cm^{-1} with a Bruker Alpha FT-ATR spectrophotometer. High resolution electrospray mass spectra (HR-ESIMS) were obtained on a Bruker MaXis Impact spectrometer, from MeCN feed solutions.

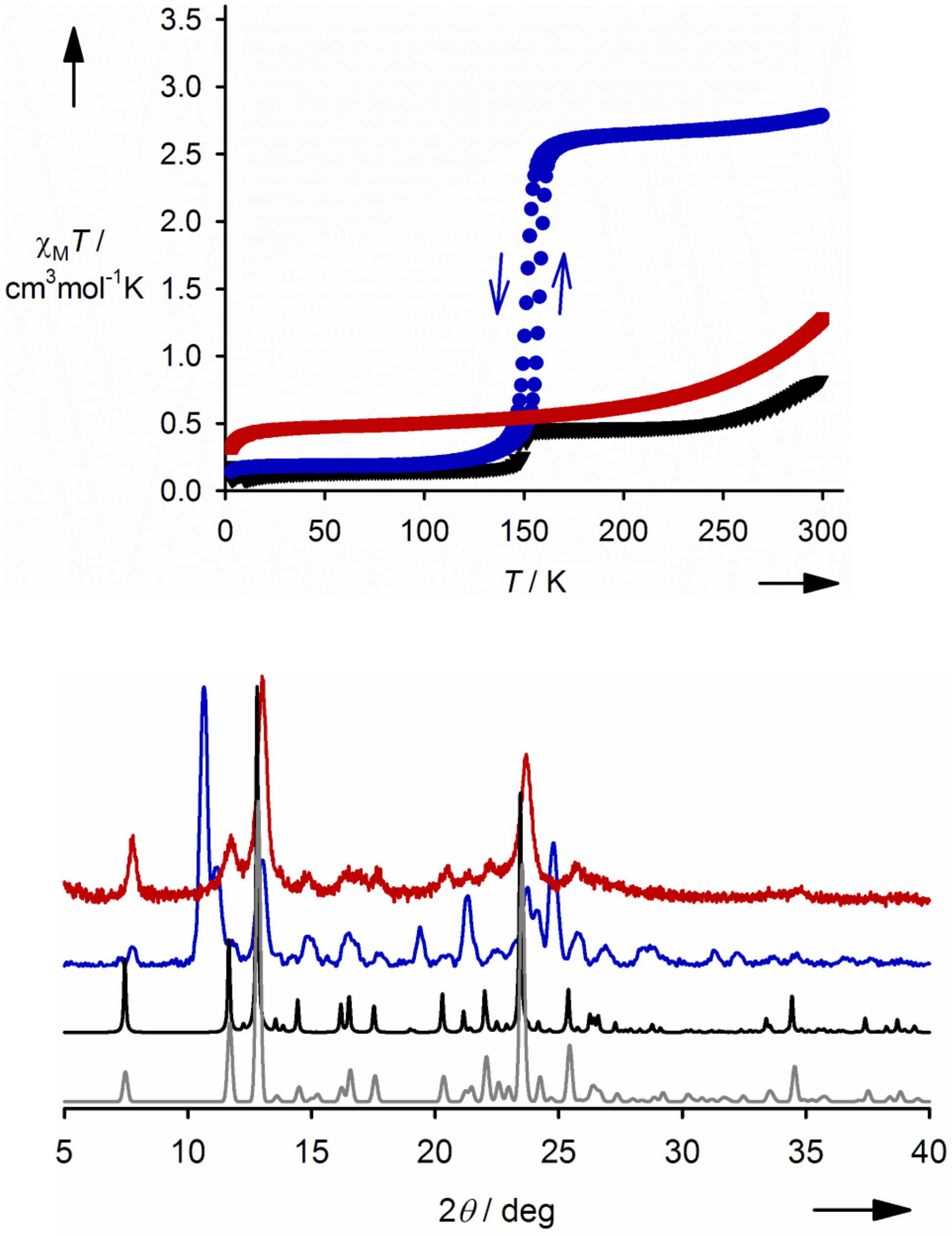

Figure S15. Variable temperature magnetic susceptibility data (top) and room-temperature X-ray powder diffraction patterns (bottom) from bulk samples of **1**: powder samples prepared by method 1 (red) or method 2 (blue); and polycrystalline material obtained by method 3 (black).

A simulated X-ray powder pattern from the solvent-free phase of **1** is also shown (gray).

The black sample is mostly crystalline, low-spin solvent-free **1** with a small fraction of an SCO-active phase evident in the magnetic data.

The red sample is much less crystalline, and seems to be *ca.* 85 % low-spin, solvent-free **1** with the reminder being high-spin amorphous material.

The blue sample is *ca.* 80 % formed of a different, unknown SCO-active phase of **1**. The remaining 20 % is low-spin, and may be solvent-free **1** (there are some peak matches with this phase in the powder pattern; Fig. S15).

The magnetic data imply that solvent-free **1** exhibits the onset of a gradual spin-transition above *ca* 250 K, which becomes more pronounced as the crystallinity of the sample is reduced. That is not evident in the single crystal structures of this phase, however.

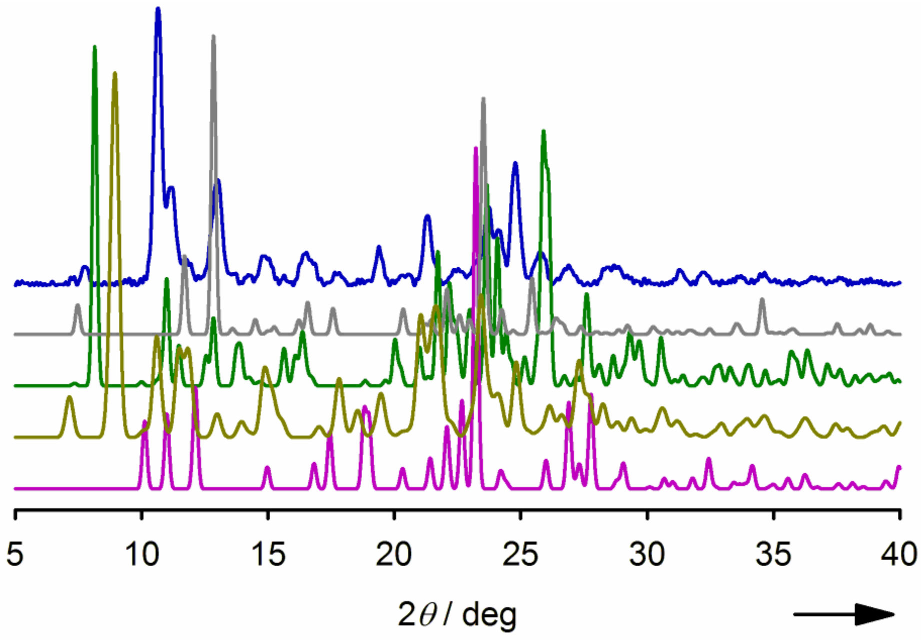

Figure S16. Comparison of the room-temperature X-ray powder pattern from **1** (method 2; blue) with simulations based on crystal structures of different phases of **1** and a related literature compound.

The simulated phases are:

1 (gray, as in Fig. S15)
1·$2C_2H_4Cl_2$ (green)
1·2py (yellow)
$[Fe(NCS)_2(phen)_2]$ (pink)[5]

The sample contains an unknown phase in *ca.* 80 % purity, that undergoes abrupt and hysteretic SCO with $T_{½}$ = 154 K, $\Delta T_{½}$ = 6 K (Fig. S15, blue curve). The powder pattern does not match any of the simulations, however, so this represents a new phase of **1** whose structure is unknown.

Many peaks in the solvent-free simulation (gray) do have counterparts in the measured powder pattern, so the low-spin solvent-free phase of **1** may form the majority of the remaining 20 % of the sample.

The SCO-active phase in this sample may be the same hydrated phase of **1** that was previously reported in the Chinese literature to exhibit SCO with a 15 K hysteresis loop.[8]

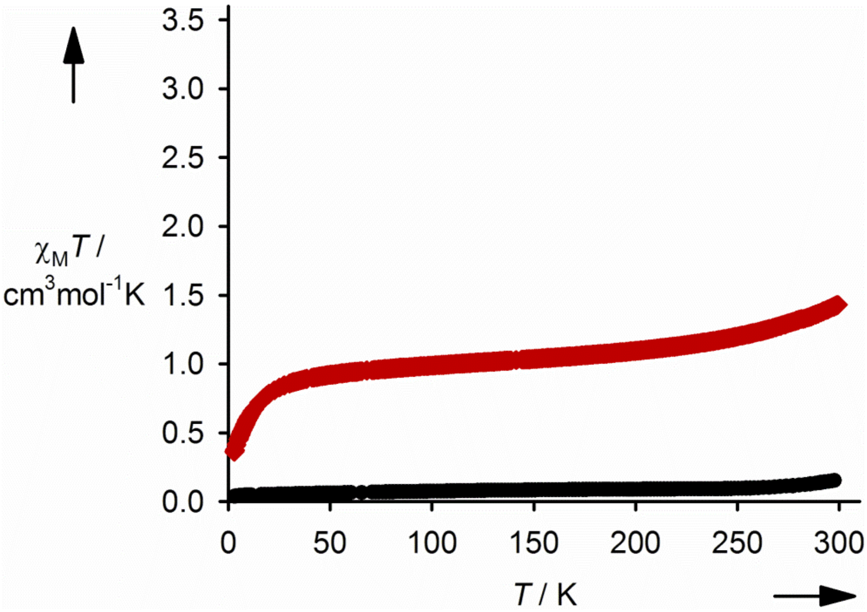

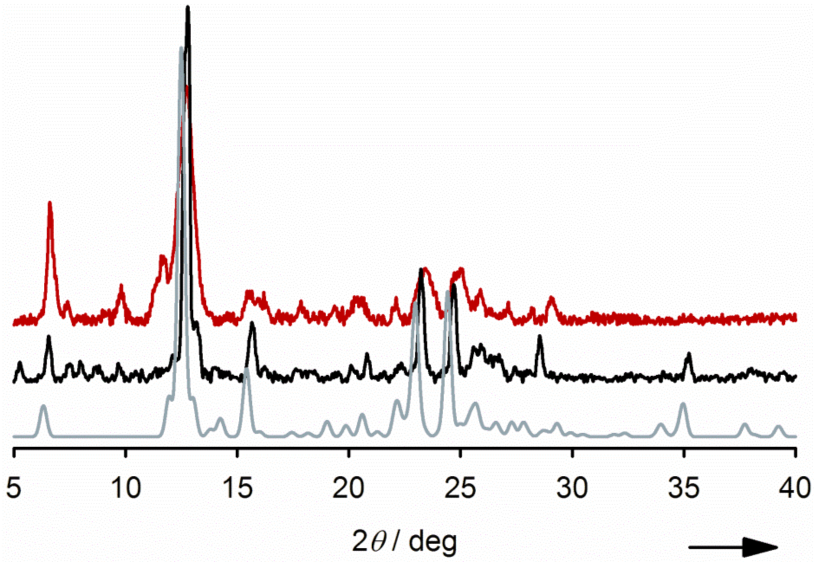

Figure S17. Variable temperature magnetic susceptibility data (top) and room-temperature X-ray powder diffraction patterns (bottom) from bulk samples of **2**: powder sample prepared by method 1 (red); and polycrystalline material obtained by method 3 (black).

A simulated X-ray powder pattern from the solvent-free phase of **2** is also shown (gray).

These data show:
Each sample predominantly contains the crystalline, low-spin solvent free phase of **2**. Both powder patterns contain extra low-angle peaks, however, that indicate the presence of at least one other contaminent phase.

As for **1**, bulk samples of **2** exhibit the onset of a gradual spin-transition above *ca* 250 K, which becomes more pronounced as the crystallinity of the sample is reduced. It is not clear whether this spin-transition arises from the contaminent phases, or from an amorphous fraction, in the samples.

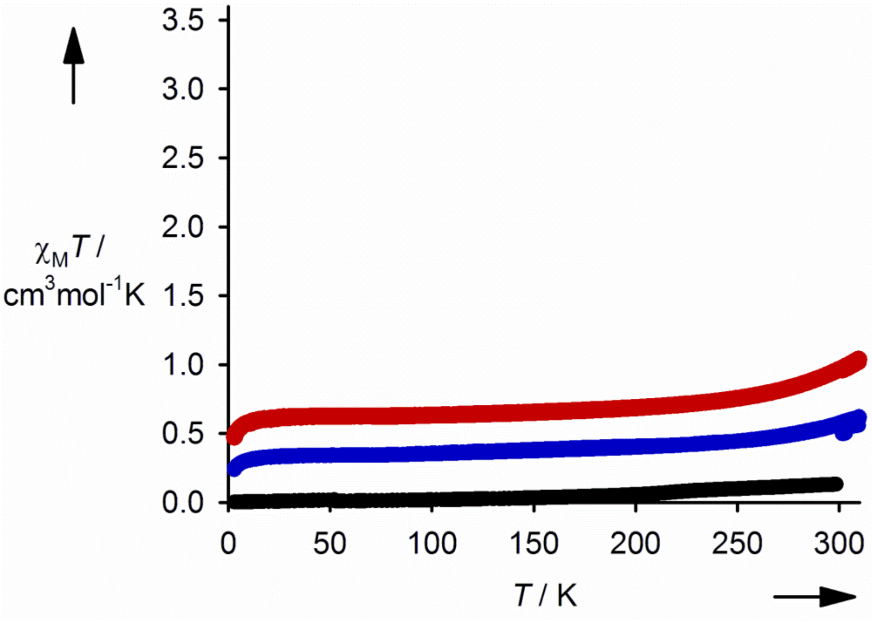

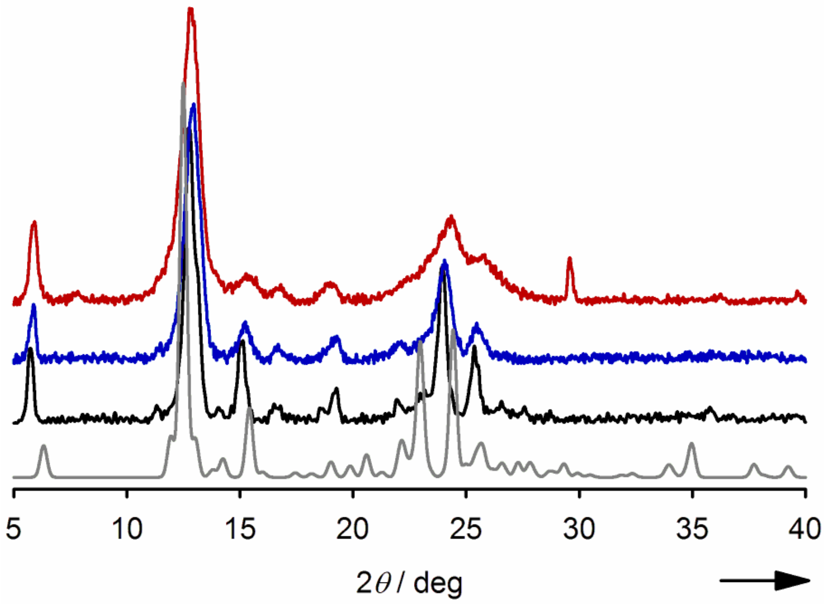

Figure S18. Variable temperature magnetic susceptibility data (top) and room-temperature X-ray powder diffraction patterns (bottom) from bulk samples of **3**: powder samples prepared by method 1 (red) or method 2 (blue); and polycrystalline material obtained by method 3 (black).

A simulated X-ray powder pattern from the solvent-free phase of **2** is also shown (gray).

All three samples have a similar phase composition, but different degrees of crystallinity. Although a crystal structure of **3** was not obtained, the resemblence between the measured powder patterns and the simulation from the structure of **2** is striking. Hence, solvent-free **3** is also low-spin, and is almost certainly isostructural with **1** and **2**. Only the red pattern has two extra peaks (at $2\theta = 7.5$ and 29.5°), indicating that a second phase may be present in that sample.

In contrast to **1** (Fig. S12), the same phase of **3** was obtained by all three methods.

As for **1**, bulk samples of **3** exhibit the onset of a gradual spin-transition above *ca* 250 K, which becomes more pronounced as the crystallinity of the sample is reduced. It is not clear whether this spin-transition arises from the contaminent phases, or from an amorphous fraction, in the samples.

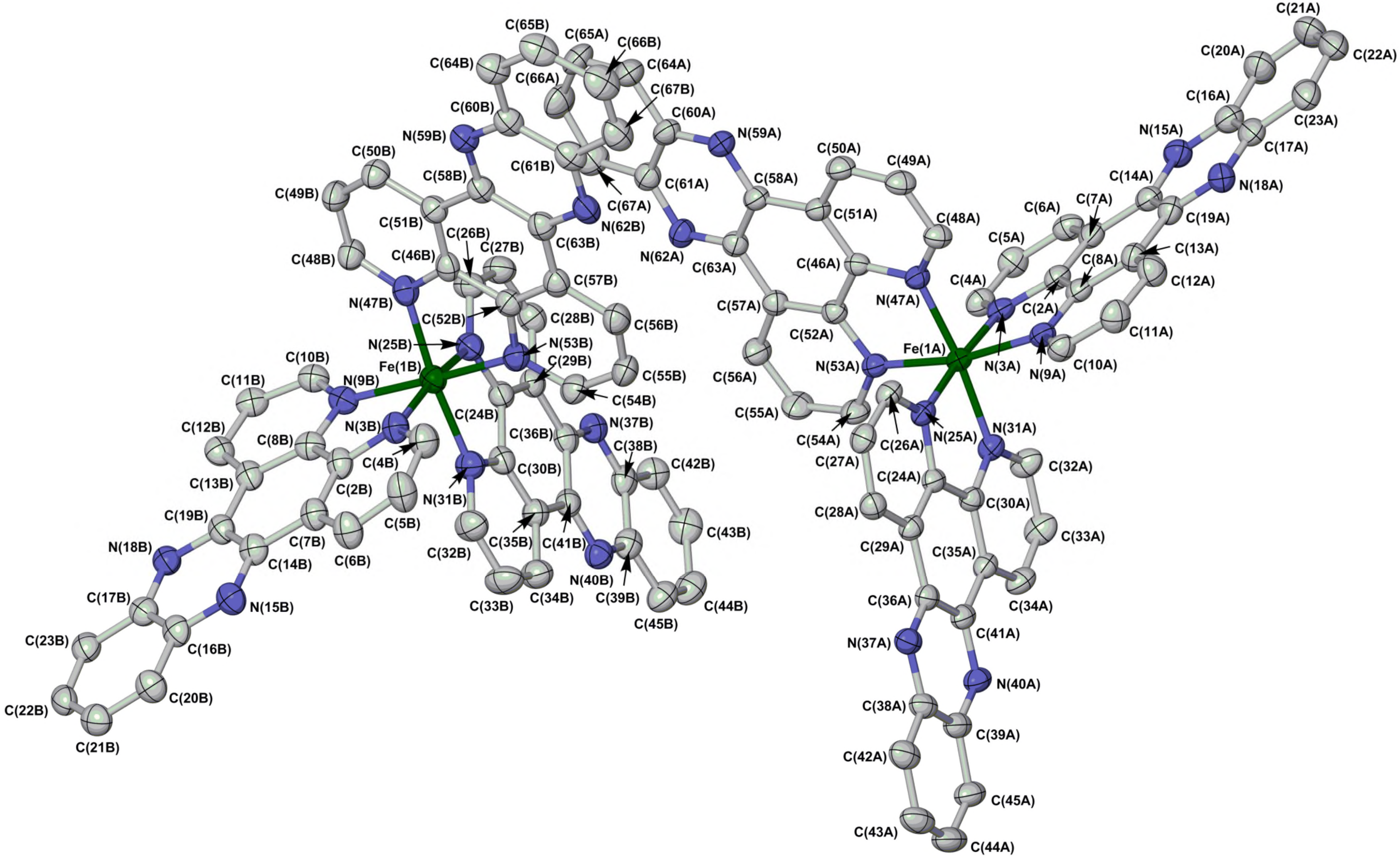

Figure S19. View of the two unique $[Fe(dppz)_3]^{2+}$ cations in **4**. Displacement ellipsoids are at the 50 % probability level, and H atoms have been omitted for clarity. Colour code: C, white; Fe, green; N, blue.

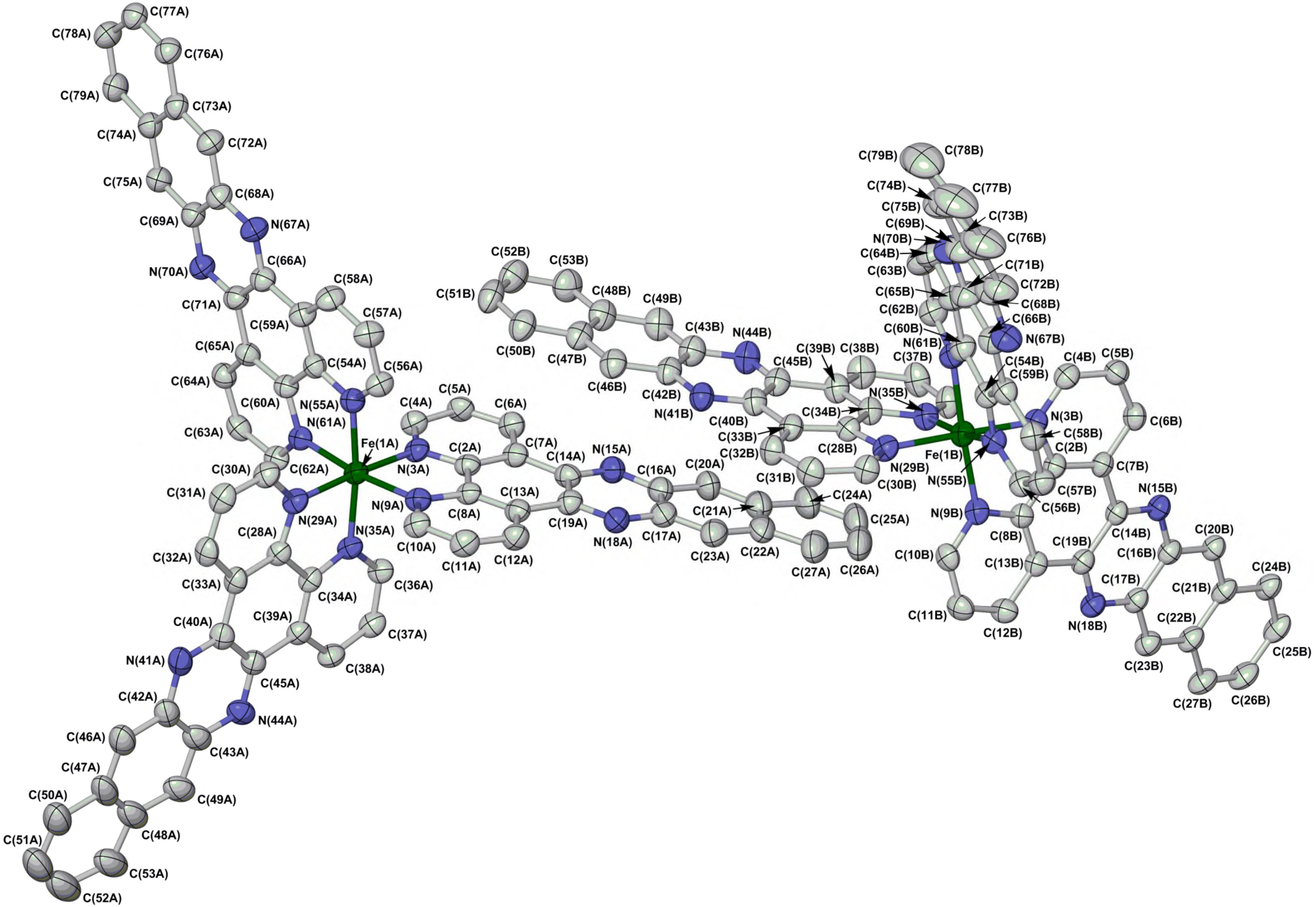

Figure S20. View of the two unique $[Fe(dppn)_3]^{2+}$ cations in **5**$\cdot$3MeOH$\cdot H_2O$. Displacement ellipsoids are at the 50 % probability level, and H atoms have been omitted for clarity. Colour code: C, white; Fe, green; N, blue. Atom C(36B) [between N(35B) and C(37B)] is not labelled for reasons of space.

Table S7. Selected bond lengths (Å) and angles (°) for the crystal structures of $[Fe(dppz)_3][ClO_4]_2$ (**4**) and $[Fe(dppn)_3][BF_4]_2\cdot 3MeOH\cdot H_2O$ (**5**·3MeOH·H_2O). See Figs S19 and S20 for the atom numbering schemes employed.

5	Molecule A	Molecule B	**5**·3MeOH·H_2O	Molecule A	Molecule B
Fe(1)–N(3)	1.989(3)	1.990(3)	Fe(1)–N(3)	1.979(4)	1.953(4)
Fe(1)–N(9)	1.987(3)	2.010(3)	Fe(1)–N(9)	1.978(4)	1.985(4)
Fe(1)–N(25)	1.981(3)	1.995(3)	Fe(1)–N(29)	1.994(4)	1.980(4)
Fe(1)–N(31)	1.981(3)	1.995(3)	Fe(1)–N(35)	1.981(4)	1.982(4)
Fe(1)–N(47)	1.980(3)	1.994(3)	Fe(1)–N(55)	1.969(4)	1.981(4)
Fe(1)–N(53)	1.986(3)	2.001(3)	Fe(1)–N(61)	1.979(4)	1.994(4)
N(3)–Fe(1)–N(9)	82.12(12)	81.48(12)	N(3)–Fe(1)–N(9)	82.01(16)	82.86(15)
N(3)–Fe(1)–N(25)	175.75(11)	169.48(13)	N(3)–Fe(1)–N(29)	176.18(15)	173.77(16)
N(3)–Fe(1)–N(31)	94.60(12)	88.46(13)	N(3)–Fe(1)–N(35)	93.92(15)	92.08(16)
N(3)–Fe(1)–N(47)	91.02(11)	93.38(12)	N(3)–Fe(1)–N(55)	93.34(16)	91.24(16)
N(3)–Fe(1)–N(53)	90.46(12)	92.30(13)	N(3)–Fe(1)–N(61)	91.79(15)	94.73(16)
N(9)–Fe(1)–N(25)	95.36(12)	94.24(12)	N(9)–Fe(1)–N(29)	97.10(16)	94.58(16)
N(9)–Fe(1)–N(31)	94.60(12)	91.73(13)	N(9)–Fe(1)–N(35)	88.79(16)	92.04(16)
N(9)–Fe(1)–N(47)	89.50(12)	94.09(12)	N(9)–Fe(1)–N(55)	94.11(16)	96.04(16)
N(9)–Fe(1)–N(53)	168.69(12)	172.38(12)	N(9)–Fe(1)–N(61)	172.56(16)	176.96(17)
N(25)–Fe(1)–N(31)	82.20(12)	82.04(13)	N(29)–Fe(1)–N(35)	90.43(16)	82.31(16)
N(25)–Fe(1)–N(47)	92.37(11)	96.52(13)	N(29)–Fe(1)–N(55)	90.43(16)	94.68(16)
N(25)–Fe(1)–N(53)	92.54(12)	92.62(13)	N(29)–Fe(1)–N(61)	89.36(16)	88.00(16)
N(31)–Fe(1)–N(47)	173.18(12)	174.10(13)	N(35)–Fe(1)–N(55)	172.49(16)	171.59(16)
N(31)–Fe(1)–N(53)	93.98(12)	92.50(13)	N(35)–Fe(1)–N(61)	95.76(15)	89.90(17)
N(47)–Fe(1)–N(53)	82.09(11)	81.83(12)	N(55)–Fe(1)–N(61)	82.10(16)	82.12(16)

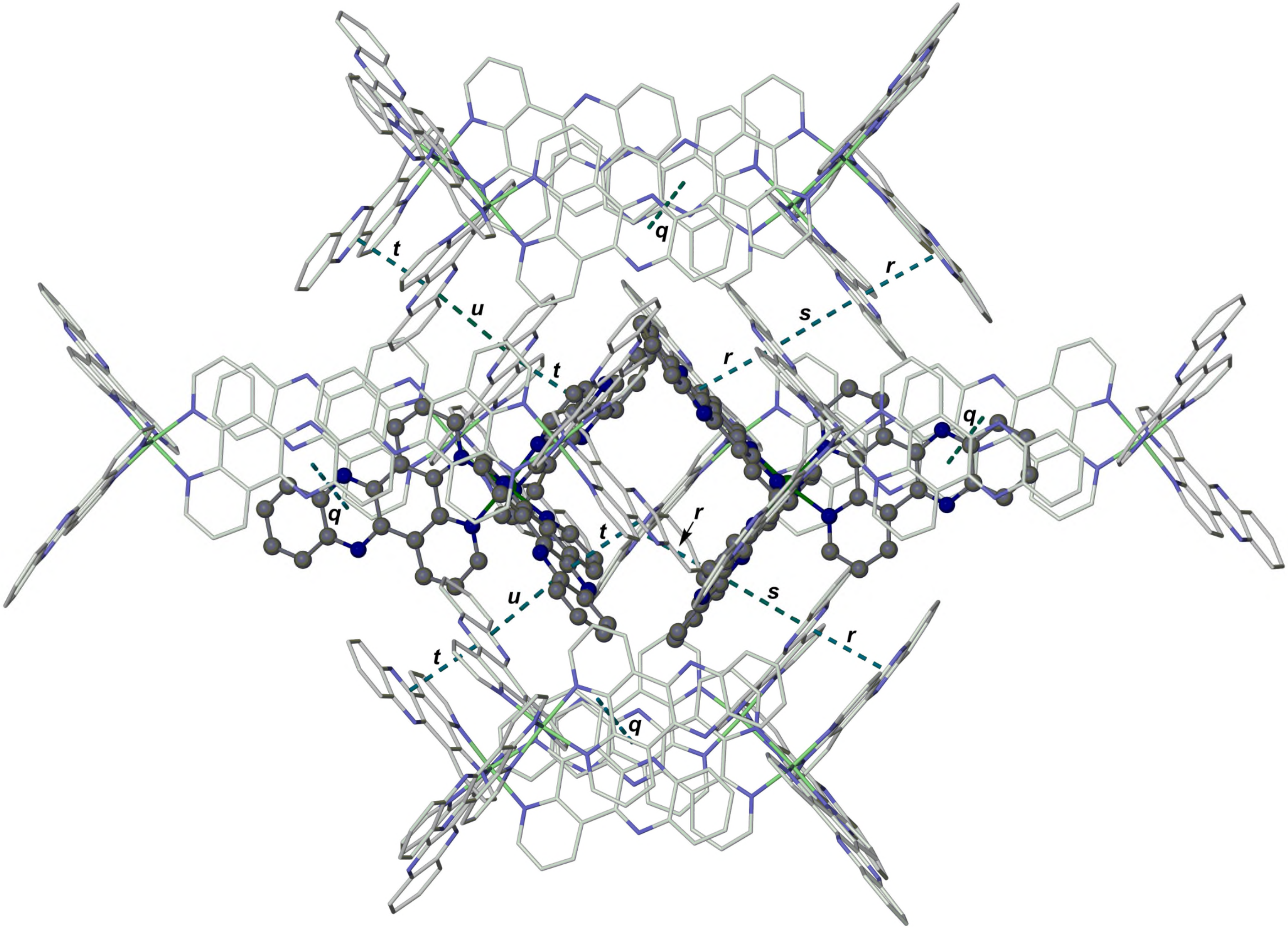

Figure S21. View highlighting the short intermolecular contacts in **4**. Metric parameters for the highlighted $\pi...\pi$ interactions are listed in Table S8.

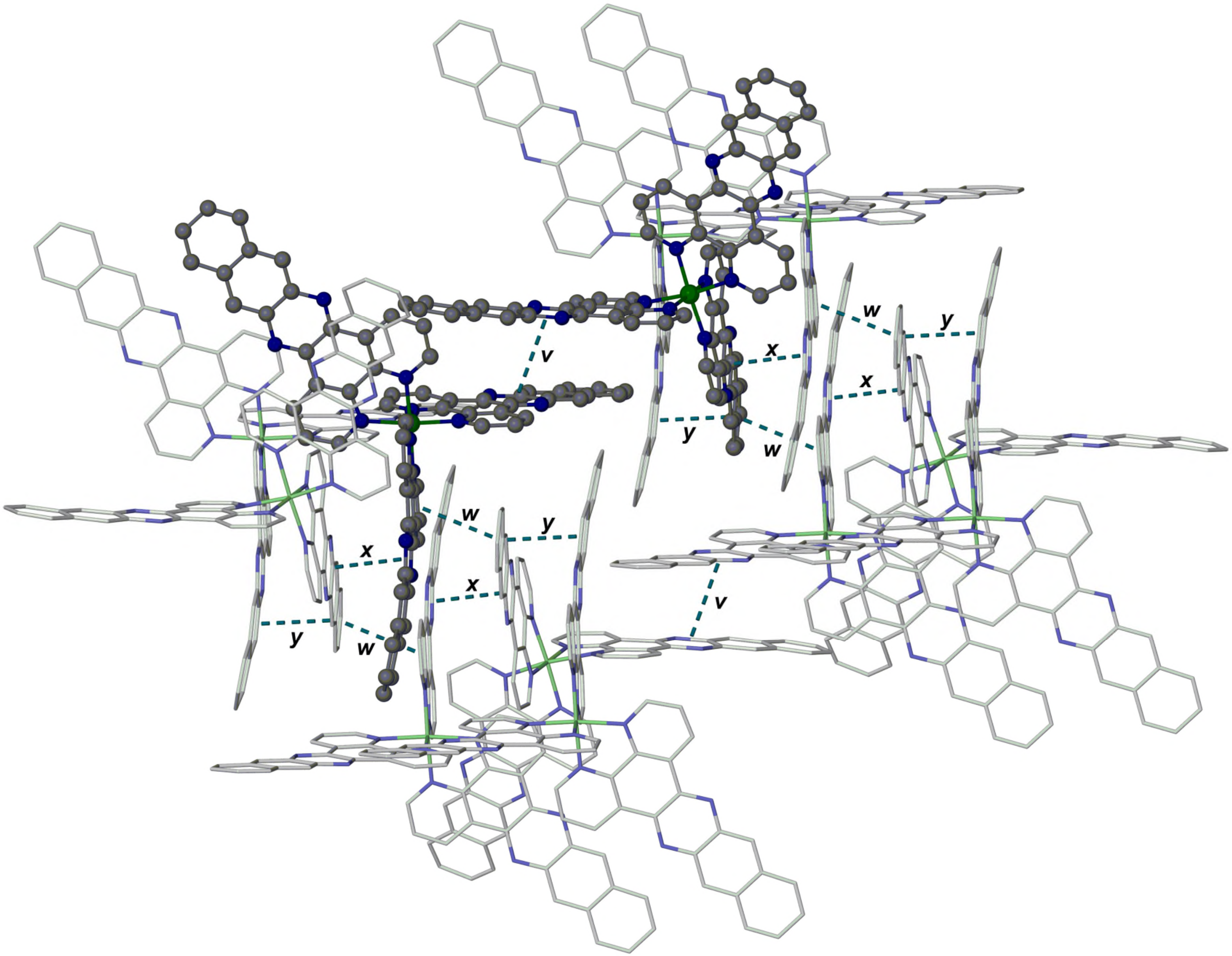

Figure S22. View highlighting the short intermolecular contacts in **5**·3MeOH·H_2O. Metric parameters for the highlighted $\pi...\pi$ interactions are listed in Table S9.

Table S8. Noteworthy intermolecular distances in the crystal structures of **4**, highlighted in Fig. S21 (Å, °). The average interatomic distance and dihedral angle between the planes of the interacting ligands are given. Symmetry codes: (xii) 1+*x*, $^{3}/_{2}$–*y*, ½+*z*; (xiii) *x*, $^{3}/_{2}$–*y*, –½+z; (xiv) 2–*x*, 1–*y*, 1–*z*; (xv) *x*, $^{3}/_{2}$–*y*, ½+*z*; (xvi) 1–*x*, 1–*y*, 2–*z*.

X(11)…X(12$^{\text{xii}}$)[a,b]	X(13)...X(14$^{\text{xiii}}$)[c,d]	X(13)...X(13$^{\text{xiv}}$)[c]	X(15)…X(16$^{\text{xv}}$)[e,f]	X(15)…X(15$^{\text{xvi}}$)[e]
q	***r***	***s***	***t***	***u***
3.62(2), 2.36(4)	3.40(2), 4.31(6)	3.49(1), 0	3.53(2), 5.23(7)	3.520(5), 0

---

[a]X(11) is the centroid of the whole dppz ligand C(2A)-C(23A). [b]X(12) is the centroid of the whole dppz ligand C(2B)-C(23B). [c]X(13) is the centroid of the whole dppz ligand C(24A)-C(45A). [d]X(14) is the centroid of the whole dppz ligand C(46A)-C(67A). [e]X(15) is the centroid of the whole dppz ligand C(46B)-C(67B). [e]X(16) is the centroid of the whole dppz ligand C(24B)-C(45B).

Table S9. Noteworthy intermolecular distances in the crystal structures of **5**·3MeOH·H_2O, highlighted in Fig. S22 (Å, °). The average interatomic distance and dihedral angle between the planes of the interacting ligands are given. Symmetry codes: (xvii) –*x*, 1–*y*, –*z*; (xviii) *x*, –1+*y*, *z*; (xix) –*x*, –*y*, 1–*z*.

X(17)…X(18)[a,b]	X(19)...X(20$^{\text{xvii}}$)[c,d]	X(19)...X(20$^{\text{xviii}}$)[c,d]	X(21)…X(21$^{\text{xix}}$)[e]
v	***w***	***x***	***y***
3.63(3), 2.43(5)	3.31(3), 3.99(7)	3.59(3), 3.99(7)	3.484(7), 0

---

[a]X(17) is the centroid of the whole dppn ligand C(2A)-C(27A). [b]X(18) is the centroid of the whole dppn ligand C(28B)-C(53B). [c]X(19) is the centroid of the whole dppn ligand C(28A)-C(53A). [d]X(20) is the centroid of the whole dppn ligand C(2B)-C(25B). [e]X(21) is the centroid of the whole dppn ligand C(54A)-C(79A).

References

[1] J. K. McCusker, A. L. Rheingold and D. N. Hendrickson, *Inorg. Chem.*, 1996, **35,** 2100.

[2] P. Guionneau, M. Marchivie, G. Bravic, J.-F. Létard and D. Chasseau, *Top. Curr. Chem.*, 2004, **234**, 97.

[3] M. A. Halcrow, *Chem. Soc. Rev.*, 2011, **40**, 4119.

[4] H. J. Shepherd, T. Palamarciuc, P. Rosa, P. Guionneau, G. Molnár, J.-F. Létard and A. Bousseksou, *Angew. Chem., Int. Ed.*, 2012, **51**, 3910.

[5] B. Gallois, J. A. Real, C. Hauw and J. Zarembowitch, *Inorg. Chem.*, 1990, **29**, 1152.

[6] C. J. O'Connor, *Prog. Inorg. Chem.*, 1982, **29**, 203.

[7] High-spin and low-spin complexes of the $[Fe(NCS)_2L_2]$ type typically exhibit $\nu_{NCS} \leq 2080$ and ≥ 2100 cm^{-1}, respectively. See *eg*:

a) R. Herber and L. M. Casson, *Inorg. Chem.*, 1986, **25**, 847;

b) R. Herber, *Inorg. Chem.*, 1987, **26**, 173;

c) P. Coronel, A. Barraud, R. Claude, O. Kahn, A. Ruaudel-Teixier and J. Zarembowitch, *J. Chem. Soc., Chem. Commun.*, 1989, 193;

d) D. C. Figg, R. H. Herber and J. A. Potenza, *Inorg. Chem.*, 1992, **31**, 2111;

e) A. A. Yousif, H. Winkler, H. Toftlund, A. X. Trautwein and R. H. Herber, *J. Phys.: Condens. Matter*, 1989, **1**, 7103;

f) C. L. Zilverentant, G. A. van Albada, A. Bousseksou, J. G. Haasnoot and J. Reedijk, *Inorg. Chim. Acta*, 2000, **303**, 287;

g) D. Zhu, Y. Xu, Z. Yu, Z. Guo, J. Sang, T. Liu and X. You, *Chem. Mater.*, 2002, **14**, 838;

h) S. Bonnet, G. Molnár, J. S. Costa, M. A. Siegler, A. L. Spek, A. Bousseksou, W.-T. Fu, P. Gamez and J. Reedijk, *Chem. Mater.*, 2009**, 21**, 1123.

[8] J.-Q. Tao, W.-Z. Shi, X. Zhuang, Z. Yu and X.-Z. You, *Wuji Huaxue Xuebao*, 2002, *1***8**, 255.